S03120100-TRT10008
ORNL/TM-2023/2912

Oak Ridge National Laboratory Heating, DPA, and He production in the Proton Beam Window Assembly for the Second Target Station

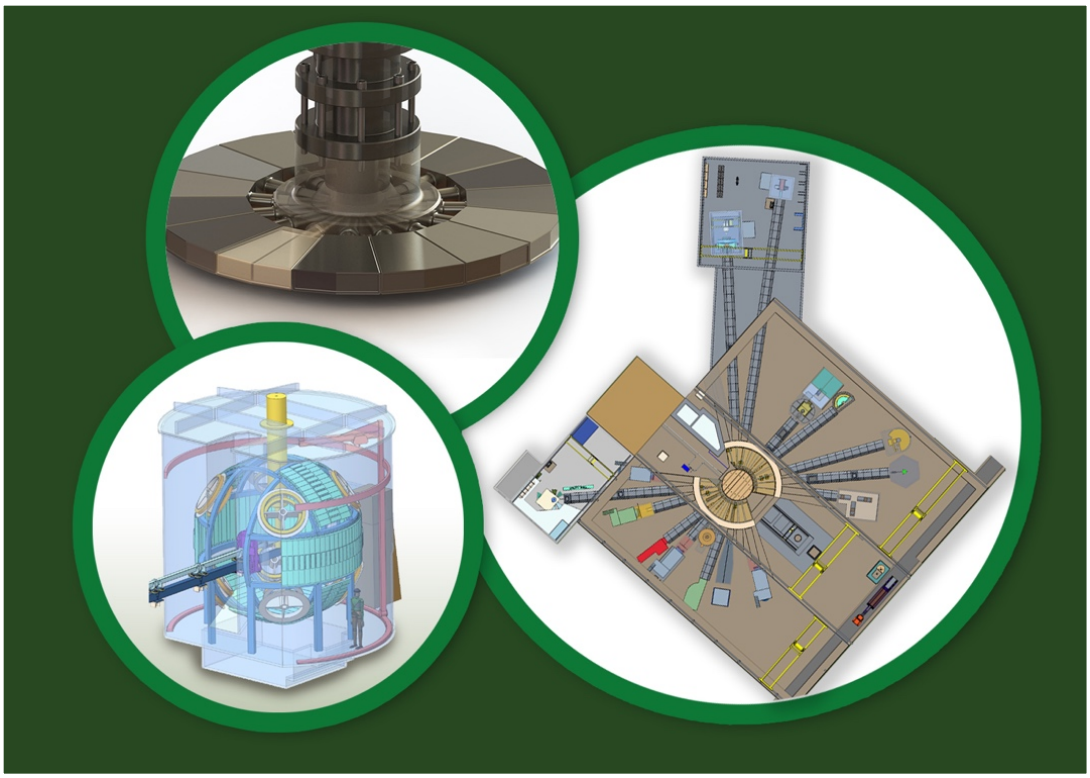

Kristel Ghoos

September 2023

OAK RIDGE National Laboratory

ORNL IS MANAGED BY UT-BATTELLE LLC FOR THE US DEPARTMENT OF ENERGY

S03120100-TRT10008
ORNL/TM-2023/2912

Second Target Station Project

HEATING, DPA, AND He PRODUCTION IN THE PROTON BEAM WINDOW ASSEMBLY FOR THE SECOND TARGET STATION

Kristel Ghoos

July 2022

Prepared by
OAK RIDGE NATIONAL LABORATORY
Oak Ridge, TN 37831
managed by
UT-BATTELLE LLC
for the
US DEPARTMENT OF ENERGY
under contract DE-AC05-00OR22725

Heating, DPA, and He production in the Proton Beam Window Assembly for the Second Target Station

LABORATORY	DIVISION/GROUP	CALC. NO.
ORNL	Second Target Station (STS) Project	S03120100-TRT10008
Prepared by	Level III Manager	Lead Engineer
Kristel Ghoos	Igor Remec	Neelam Pradhan

Other WBS elements affected: S031201

	Signature/Date			
	REV 0	REV 1	REV 2	REV 3
Prepared by				
Task Leader				
Level III Manager				
Checked by				
Lead Engineer				

CONTENTS

LIST OF FIGURES

LIST OF TABLES

ABBREVIATIONS

ORNL	Oak Ridge National Laboratory
CSG	Constructive Solid Geometry
PBW	Proton Beam Window
SNS	Spallation Neutron Source
STS	Second Target Station Project
UM	Unstructured Mesh

EXECUTIVE SUMMARY

This report details the analysis of the heating rates, dpa values, and He production in the Proton Beam Window (PBW), the assembly around the PBW, and the shielding above it.

Neutronics calculations use a detailed Unstructured Mesh (UM) converted from the solid CAD model of the PBW design of June 2022. The rest of the geometry is taken from the CSG master model (as of June 2022). For this analysis, a proton beam profile with a footprint of ≈90 cm^2 has been used. This proton profile was created by a Ring to Second Target magnet array configuration using octupole magnets.

Maximum values in the PBW (aluminum) are 5.4 J/cc/pulse heating rate, 1.1 dpa per year, and 660 appm He-production per year. These results within ~ 10% with the previous calculations from June 2020 [1].

Average heating and dpa rates have been calculated for each component in the PBW assembly and will be used to evaluate and design the cooling needs and make decisions on removable components for the PBW. It is desirable to optimize and simplify the PBW design by only replacing components that are at the end of their lifetime.

Additional analysis for the energy deposition in the PBW is performed for two super-Gaussian beam profiles with a footprint of 60 cm^2 and 30 cm^2 respectively. Also, an estimate of the PBW lifetime is performed for two realistic quadrupole beam profiles.

1. SCOPE

This analysis covers the energy deposition, dpa rates and He-production rates in the Proton Beam Window (PBW) Assembly of the June 2022 STS design. This is in response to Neutronics Task Order 37. This analysis includes the results of revision 1 of this task order, which was performed in 2023.

2. ACCEPTANCE CRITERIA

The output of this analysis required first order of magnitude heating rates (as specified in the task order). The model is detailed and can, therefore, be considered high-fidelity analysis, giving accurate values. However, no variance reduction has been used, which results in relatively large statistical errors in some parts of the domain. This is expected to be sufficient for the analysis.

An excellent agreement has been observed comparing the results of this analysis with previous results, which gives confidence in its reliability.

3. ASSUMPTIONS AND LIMITATIONS

A proton beam profile with a footprint of ≈90 cm^2 has been used. This proton profile was created by a Ring to Second Target magnet array configuration using octupole magnets. Proton beam losses of 1 W/m have not been considered.

4. METHODOLOGY AND MODELS

This analysis uses the STS master model (pulled from the master branch on June 6, 2022). An impression of a part of the geometry is shown in Figure 1. This version does not have a Target Viewing Periscope (void instead). The CSG geometries are used for all components except the PBW (universe 50, UM1) and its upper shielding (universe 51, UM2). For these components, an unstructured mesh has been generated using Attila4MC, based on the SpaceClaim file 'PBW-Assembly-Prelim-Geom-ver2.2 - With Materials' located in sts_archive/0-Task-Orders/TO-037_S.03.05_2022-04-05_PBW_HEATING/2-SPACECLAIM on Saturn.

The small round water channels (3mm diameter) that cool the PBW have been replaced with **square water channels with the same volume**. This allows for a coarser meshing without significantly changing the total water volume. This is illustrated in Figure 2. Table 1 lists the volume in the SpaceClaim files and in the final mesh. The 3% loss in the mesh is mostly in the larger channels on the side, and not in the small (square) channels that pass through the center of the PBW.

Table 1: Comparison of volume in the water channels of the PBW for the original SpaceClaim file, the simplified SpaceClaim file, the mesh with rounded channels and the mesh with square channels.

	Volume of the PBW water [cc]
Original SpaceClaim file	1312.5
Simplified SpaceClaim file (square channels)	1309.5 (-0.2%)
Unstructured mesh MCNP model with rounded channels	1298.98 (-1%) with 176,123 cells
Unstructured mesh MCNP model with square channels	1270.64 (-3.2%) with 8,544 cells

To further facilitate the meshing, the SpaceClaim-file has also been simplified by removing chamfers, rounded corners, etc. The file that has been used for the mesh of the PBW is box50_cut_del_waterchannels_3. Tables detailing the volumes in the original SpaceClaim file, the simplified SpaceClaim file and the final mesh from Attila4MC can be found in appendix D.

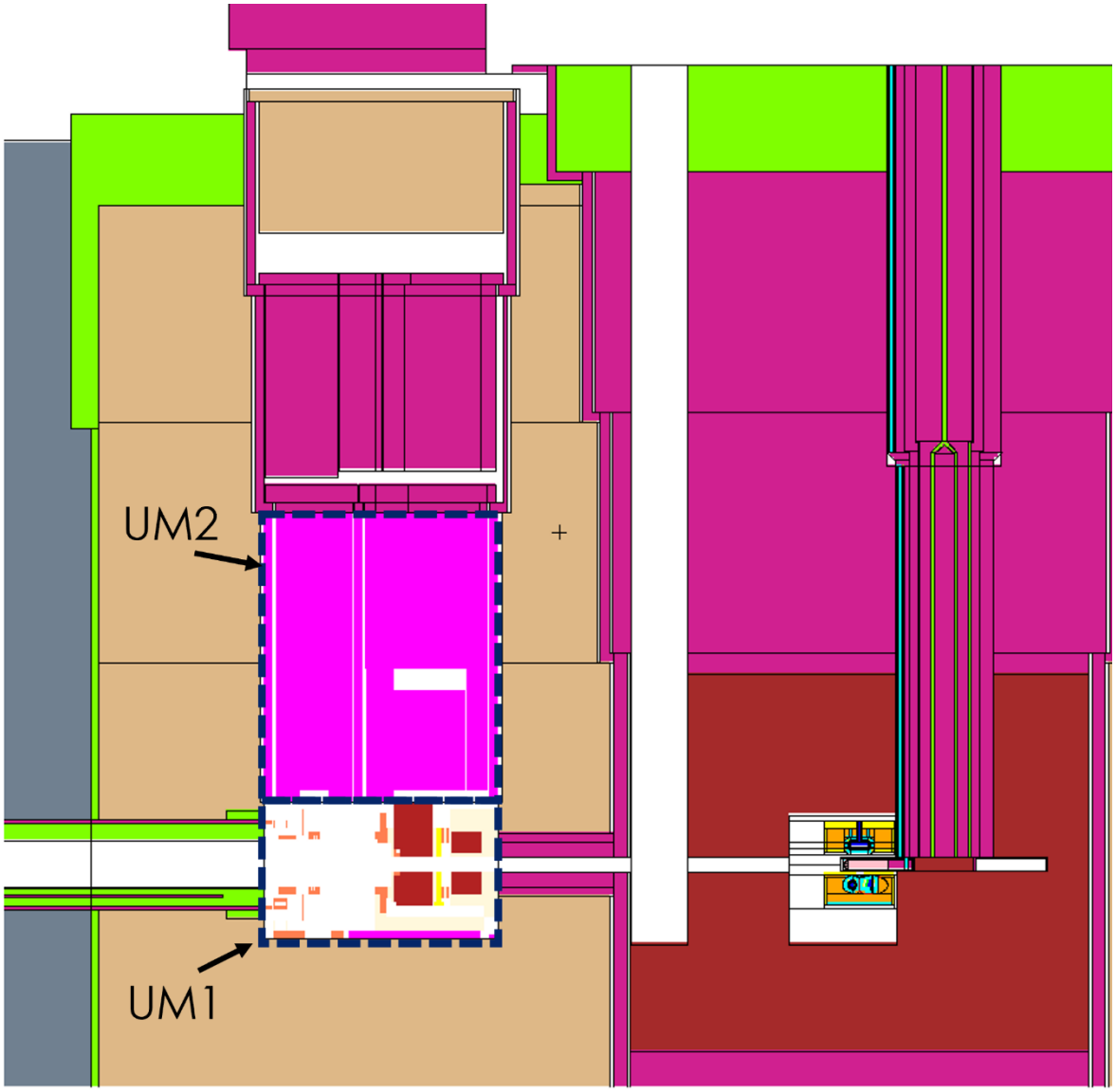

Figure 1: Impression of the geometry of the master model with two unstructured meshes, UM1 and UM2, for the proton beam window assembly and the shielding above it respectively

The following meshing parameters in Attila4MC have been used: 10 cm max edge length overall, 2 cm in the thin section of the PBW which is in direct contact with the proton beam, 4 cm in the rest of the PBW and the water channels inside the PBW. This gives a mesh with 64,138 mesh cells, of which 8,544 cells are used to describe the water in the PBW and 26,151 to describe the PBW itself (4,970 in the thin part and 21,181 in the thick part). Curvature refinement (anisotropic) is turned on with a transition factor of 0.2 and a minimal edge length of 1 cm.

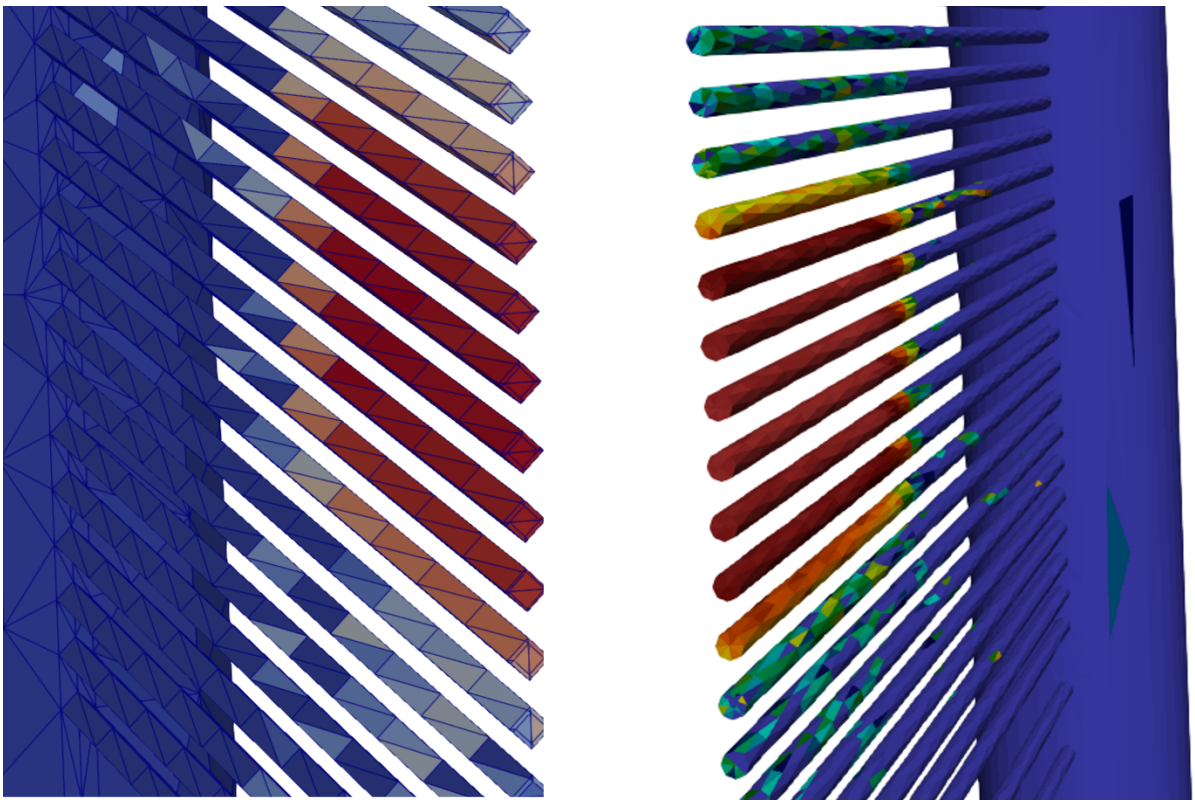

Figure 2: Impression of the mesh with square water channels (left) and a mesh created with round water channels (right). With round water channels, a very large number of mesh cells is needed to capture the geometry well. This slows the MCNP simulation down and requires more particles to reach a reasonable statistical error in each mesh element. As this level of detail is unnecessary for this study, the round channels have been replaced with square channels of the same volume.

The maximal edge lengths have been chosen to obtain sufficient statistics in a reasonable time without the need for variance reduction. The MCNP simulation for energy deposition used 2e7 particles, which takes ≈20 h on 8 nodes of Saturn. The simulations for the dpa rates and He production have been run with 1e7 particles.

The proton beam source starting 1060 cm upstream of the target has been used (octo_sampled_source_d_1060_cm_source_arrays.txt). Beam losses of 1 W/m along the proton beam are not considered in this analysis. For the super-Gaussian beam profiles used in Section 6.1, a horizontal and vertical standard deviation of respectively 5.17 cm and 1.98 cm is used for the 60 cm^2 profile, while 3.04 cm and 1.65 cm is used for 30 cm^2 profile. For the quadrupole sources used in Section 6.2, the appropriate source_arrays.txt are used as described in that section.

Several materials have been used to model the PBW assembly and its shielding. Material choice and density is taken as indicated in the component descriptions in the SpaceClaim file. The PBW is modeled as aluminum Al6061 with a density of 2.7g/cc. It is cooled with light water with a density of 0.997 g/cc. The components in the PBW assembly are mostly stainless steel, either SS316 or SS316L, with a density of 8.0 g/cc. The cooled components (cooled shielding and collimator) consist of a homogeneous mixture of 90% SS316L and 10% water with a density of 7.2998 g/cc. The upper shielding is modeled as steel A36 with a density of 7.8 g/cc.

The energy deposition in the mesh is calculated as the sum of the contributions of the protons, neutrons, photons, deuterons, tritons, alpha particles, and positive pions. The average energy deposition in the

components (calculated using +F6 tallies) considers all simulated particles. For the PBW, the two values differ by only 2%. The total energy deposition in the mesh is 92.018 J/pulse, and the total energy deposition from the + F6-tally is 94.088 (+2%). We conclude that the considered particles species in the mesh cover most of the energy deposition.

When protons interact with the material (as happens in the PBW and the components close to the PBW downstream), ionization losses are responsible for most of the energy deposition. If the energy deposition is not dominated by protons, then photons give the highest contribution. The contribution of neutrons is small through the whole PBW assembly.

The +F6 tally value, given in **MeV/g per proton**, is multiplied by its corresponding volume element mass (in g, given in the output of the tally), scaled by 1.602e-13 (conversion from MeV to J), scaled by 2.24e14 (protons per pulse for the 700 kW 15 Hz operation), divided by the volume (in cc, given in the MCNP output file). This results in the final heating rate value in **J/cc/pulse**.

To calculate the dpa, the neutron and proton fluxes are scaled by flux-to-dpa conversion factors [2-5]. More details can be found in appendix C and in the MCNP input files. Three sets of conversion factors have been used:

- flux-to-dpa in SS316, which has been used for the components in SS316, A36, and a combination of SS316 and water.
- flux-to-dpa in aluminum, which has been used for all components in Al6061
- flux-to-He-production in aluminum, which has been used for all components in aluminum Al6061.

The reported values for dpa have been scaled from the F4 tally results. The total dpa (in **dpa per pulse**) includes the sum of the neutron and proton dpa, multiplied by 2.24e14 (number of protons per pulse), and multiplied by 1e-24, which converts the cross-sections from barns to cm^2, which is necessary because the flux is given in cm^{-2}. To convert to **dpa per year**, we assume 5000 hours of operation (15 Hz) at full power per year. The He-production is reported in appm (and therefore includes an additional scaling factor of 1e6).

For the visualization of the results, we have used Paraview 5.10.0-RC1. The MCNP UM tally results have been converted to hdf5 format using a Python script [6].

5. ANALYSIS AND RESULTS

5.1 ENERGY DEPOSITION

The maximum energy density in the PBW is 5.4 J/cc/pulse. This result is similar to the previous results obtained with a 90cm^2 "quadrupole" beam (4.0 J/cc/pulse). The "octupole" beam has a different shape than the quadrupole beam, but also has a footprint of ≈90cm^2 and exhibits similar peak current values. Similar results are therefore expected. The energy deposition in a YZ-plane through the middle of the PBW can be seen in Figure 3. The energy deposition in the whole PBW assembly and its shielding can be seen in Figure 4. The statistical errors are converged in the regions of the highest energy deposition (with statistical errors <10%). In the regions upstream of the PBW, in the upper left region of the shielding, and in the region of the PBW that doesn't interact directly with the proton beam, errors are larger. These results should be used with caution and give only an indication of the order of magnitude, which is sufficient for the current analysis. More details on the statistical errors of these results can be found in appendix E.

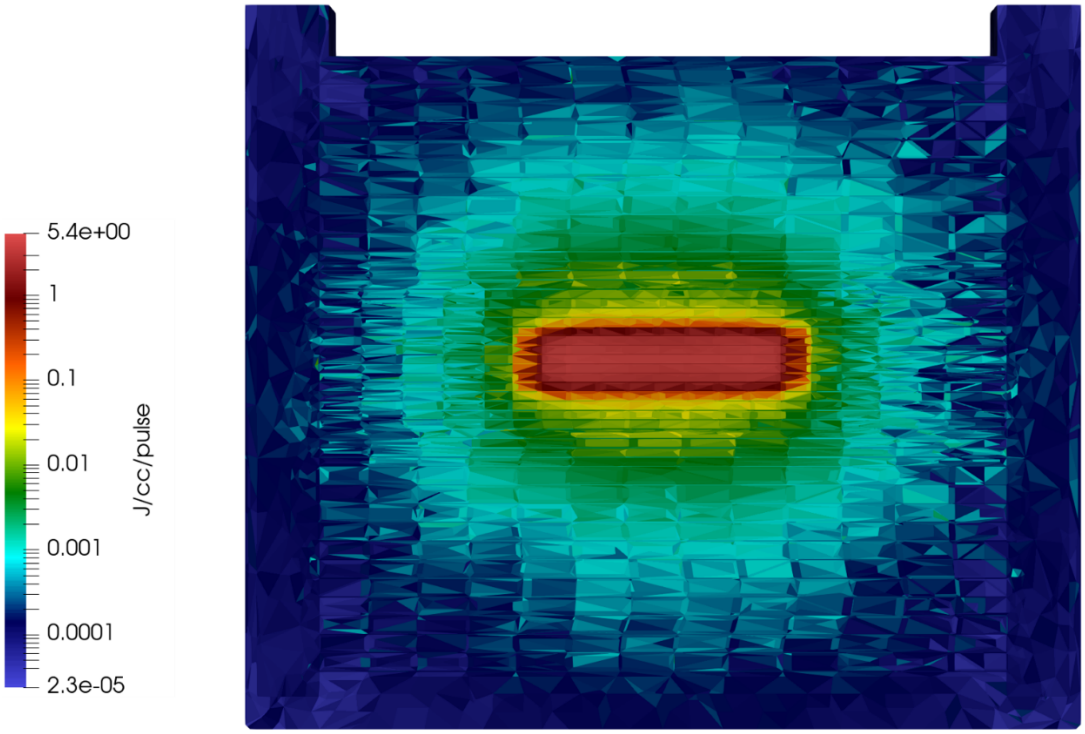

Figure 3: Energy deposition in a YZ-plane through the middle of the PBW.

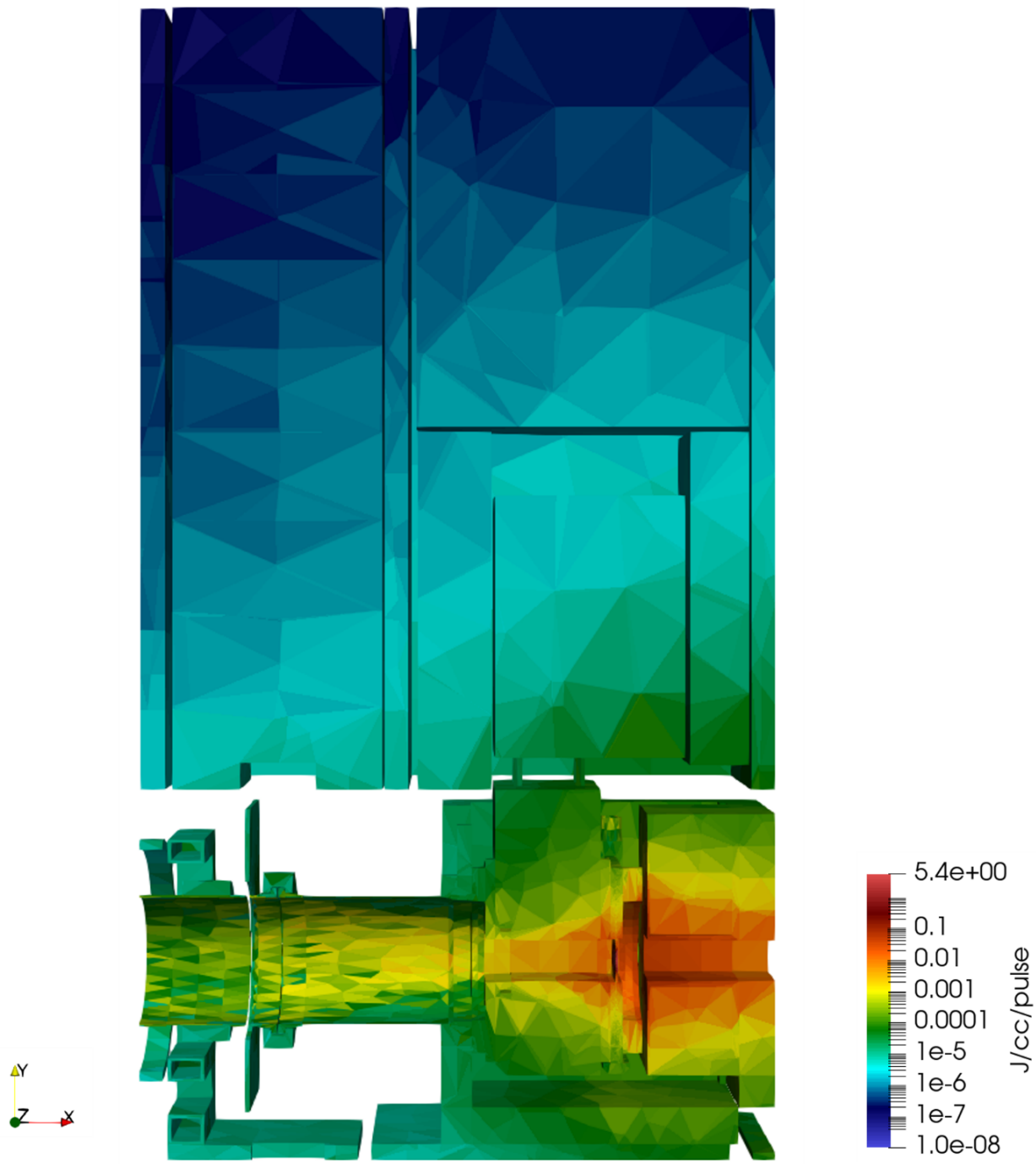

Figure 4: Energy deposition in the PBW assembly and shielding.

The average heating rates per component are listed in Table 3. In Figure 5, the most interesting components are pointed out with their average heating rates.

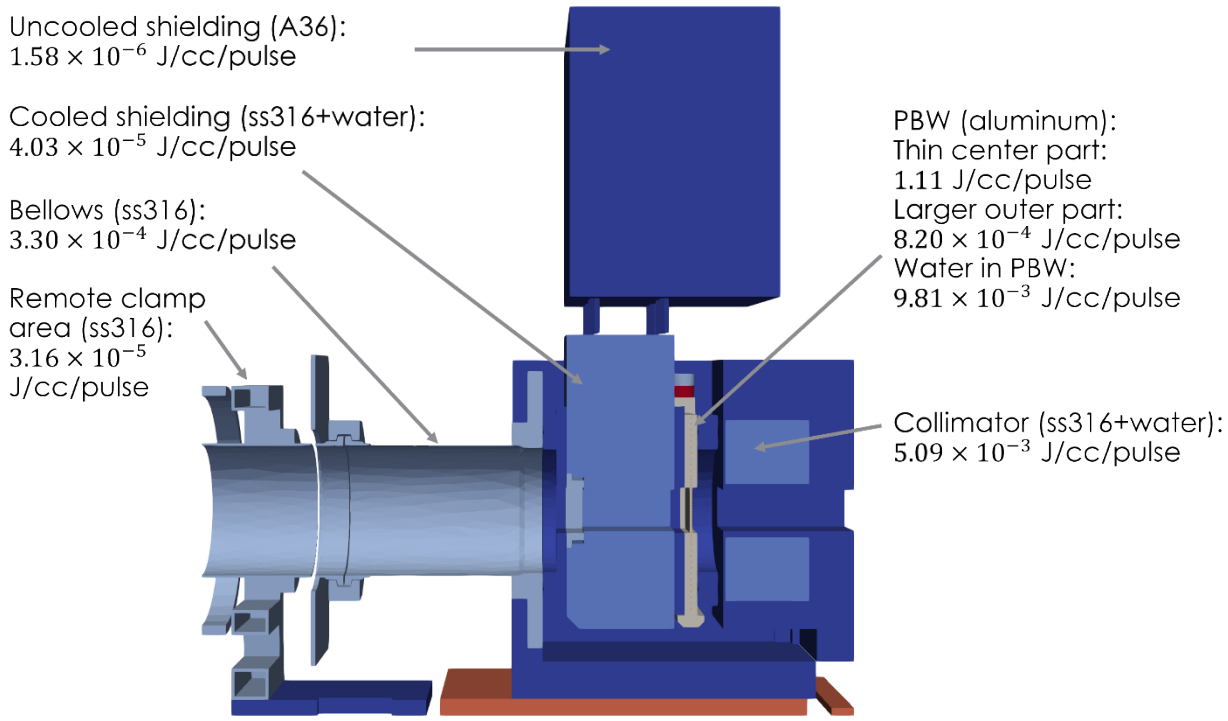

Figure 5: Average energy deposition in main components. Full details for all components can be found in Table 3.

5.2 DPA AND He-PRODUCTION

The results of the dpa calculation in the PBW assembly are graphically shown in Figure 6. The dpa and He-production rates in a YZ-plane through the middle of the PBW can be seen in Figure 7 and Figure 8 respectively. The statistical errors of these results are graphically shown in Figure 18, Figure 19, and Figure 20 in appendix E.

For the lifetime of the PBW, the maximum dpa and He-production rate are the limiting factors. With a maximum of 1.1 dpa per year and 660 appm He per year, the expected lifetime is calculated to be respectively 36 and 3 years. The He-production is clearly the dominant contributor. It is interesting to compare these results to those obtained in June 2020. These have been obtained with a 62cm^2 beam and a PBW of 10 mm thickness. The results of July 2022 use the octupole beam and a 5 mm thick PBW. The previous maximal values in the PBW are 616 appm He-production and 1.07 dpa per year. This is very similar to the results of this analysis. A summary of the comparison can be found in Table 2.

Table 2: Comparison of results between June 2020 and July 2022

	Result June 2020	Results July 2022	Lifetime limit
Maximum He rate	616 appm per year	660 appm per year	2000 appm ➔ 3 years
Maximum DPA rate	1.07 per year	1.1 per year	40 dpa ➔ 36 years

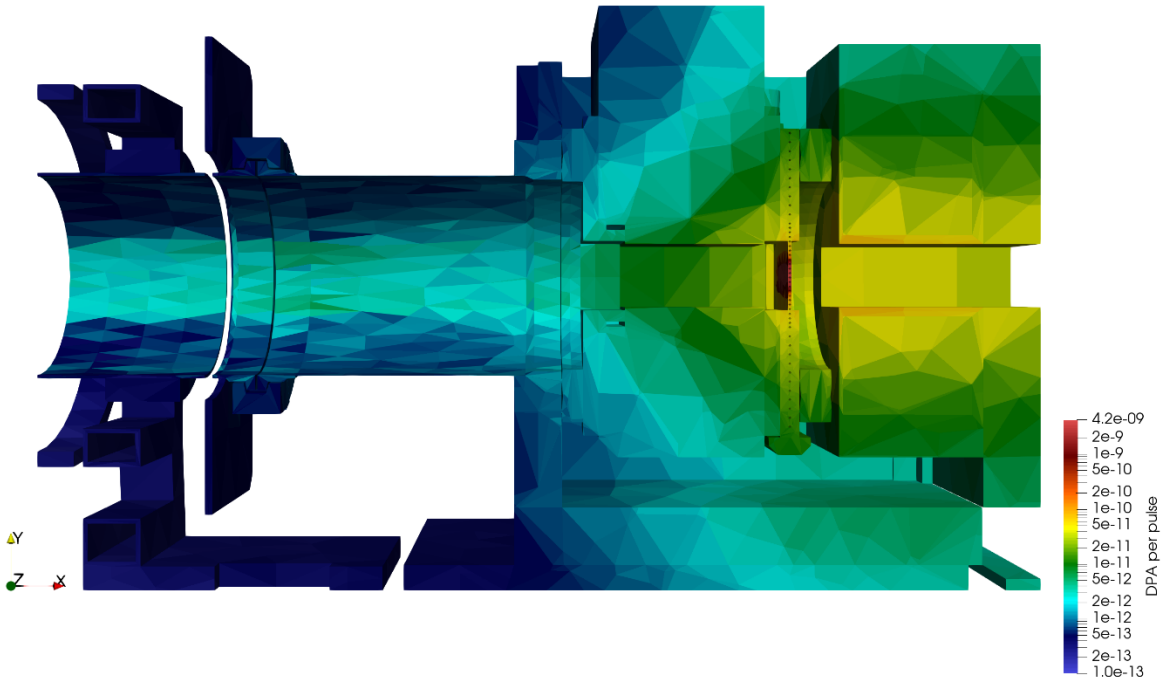

Figure 6: DPA in the YX-plane through the middle of the PBW assembly

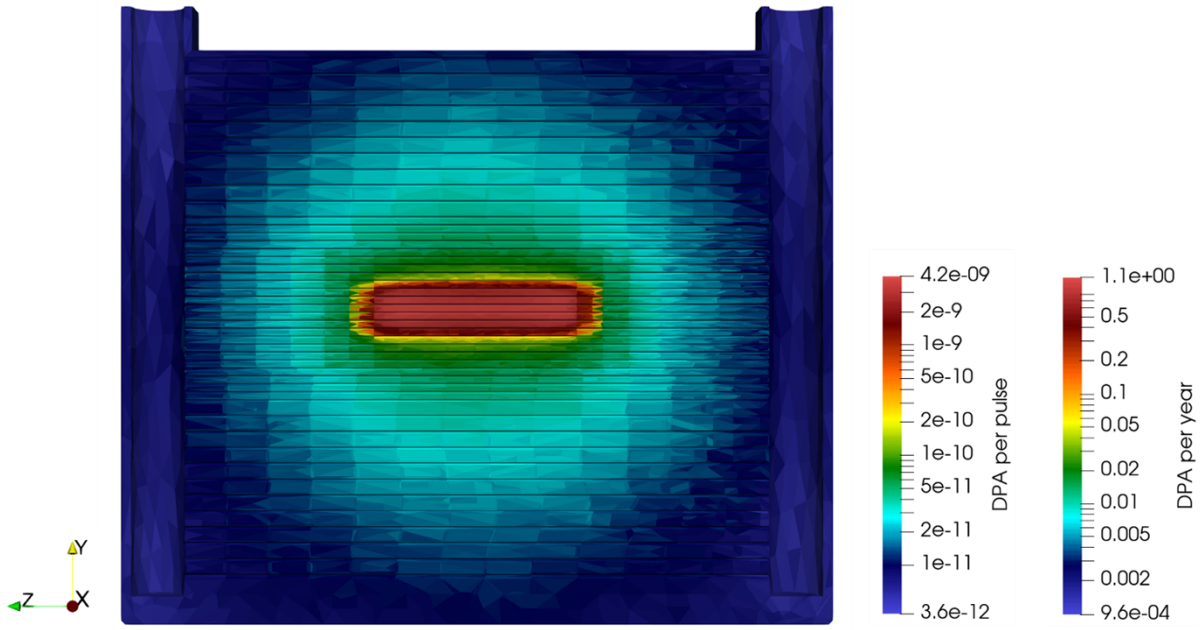

Figure 7: DPA in a YZ plane through the middle of the PBW

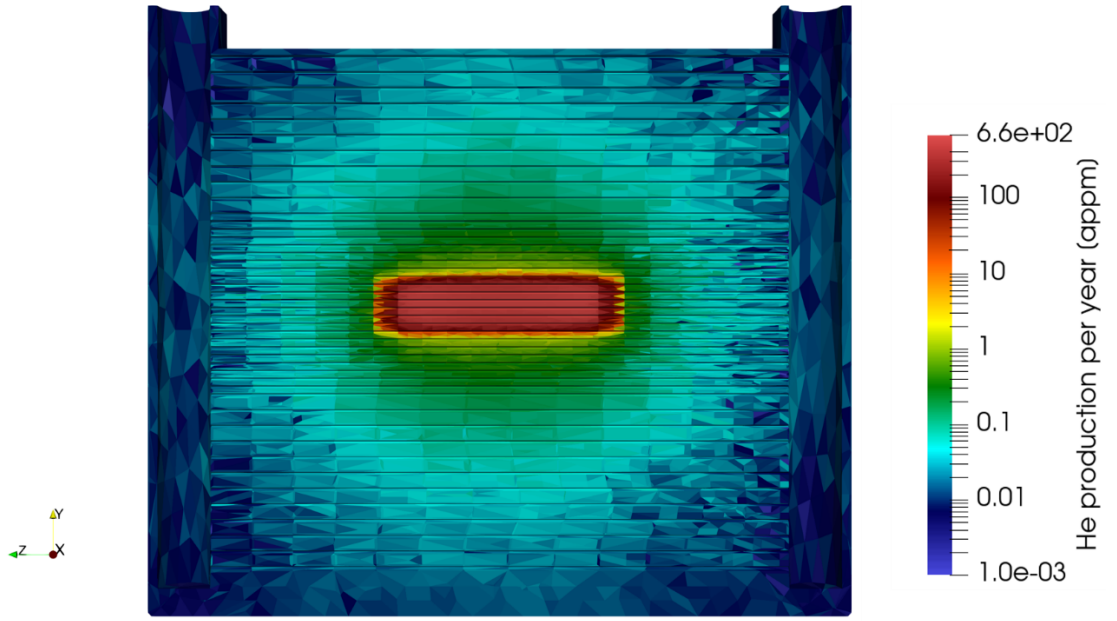

Figure 8:He-production [appm per year] in a YZ-plane through the middle of the PBW

The average dpa values per component are listed in Table 4. The average He-production rate in the aluminum components are listed in Table 5. In Figure 9 the main components are pointed out with their average value. In Figure 10, the maximum dpa values are listed for the main components. Additional maximal values can be extracted from the data (available in the STS archive, see Appendix B).

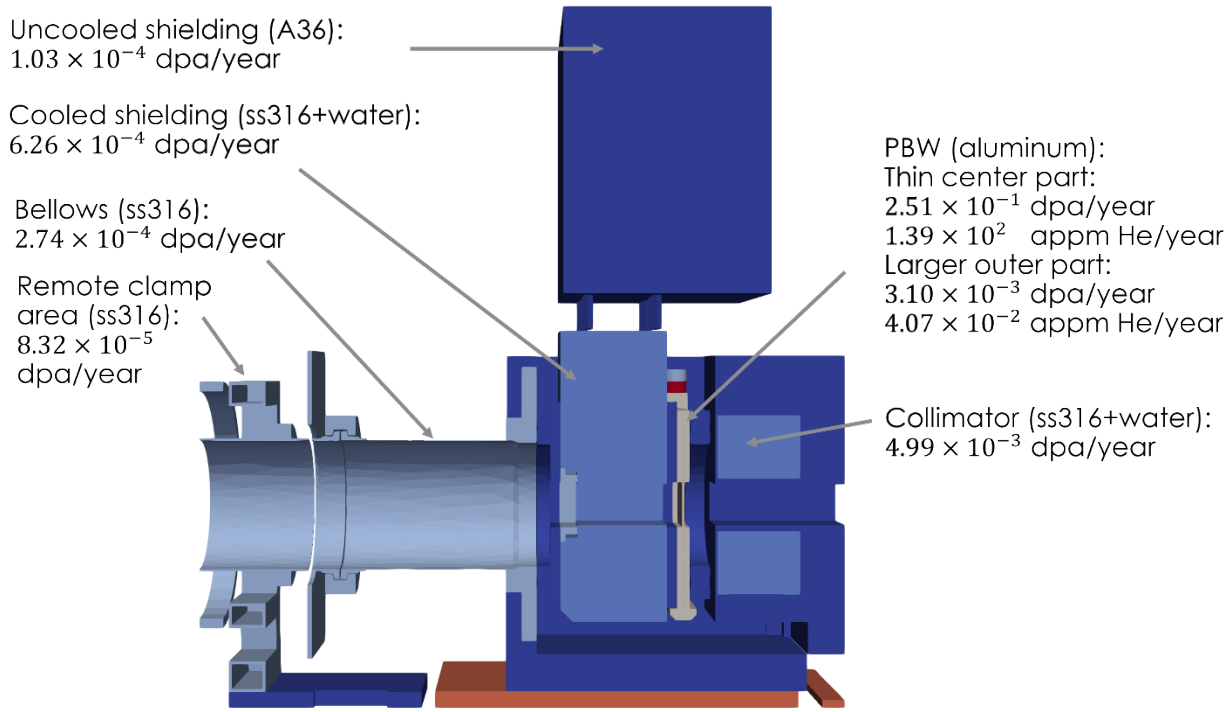

*Figure 9: **Average** DPA and He-production rates in main components. Full details for all components can be found in Table 4.*

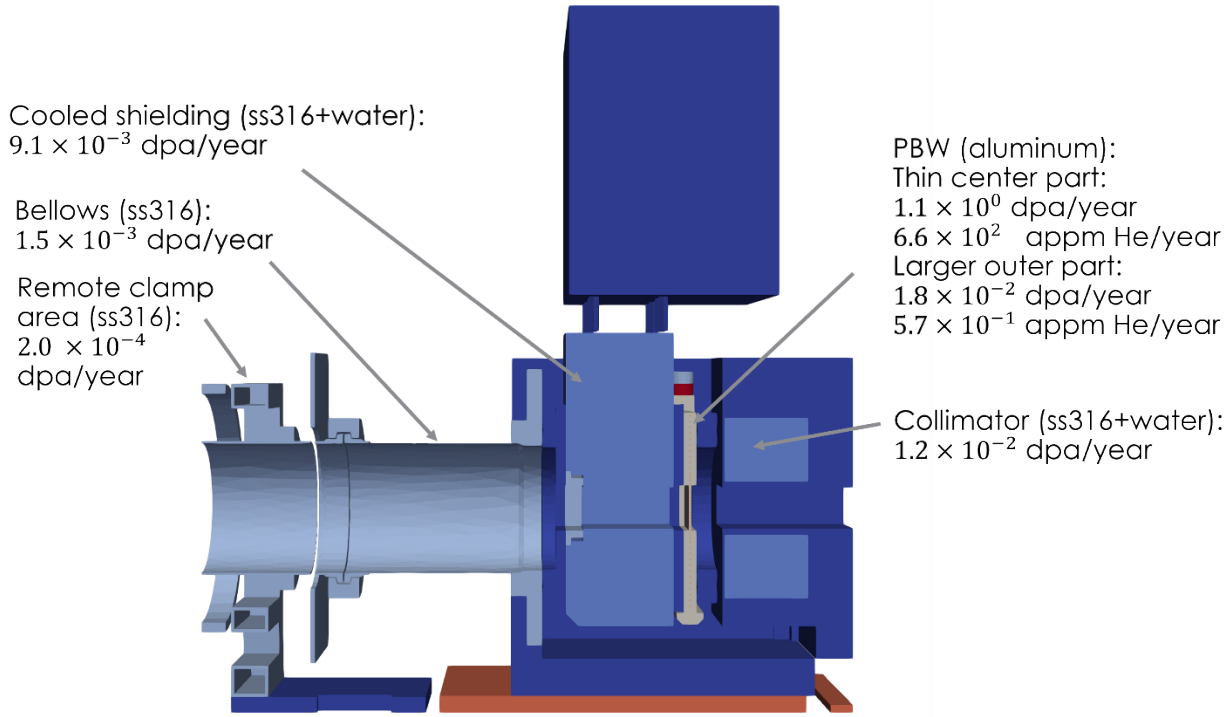

*Figure 10: **Maximum** DPA and He-production values in main components.*

Table 3:Average energy deposition in each part

Part name in SpaceClaim	Cel in MCNP	+F6 tally (MeV/g)	Relative Error (-)	Total J per pulse	J/cc/pulse
solid-matsts_316l_ss_90_h2o_10rho-7.299823P1	7000001	1.12E-06	0.0038	1.914E+01	4.03E-05
s03050121-m8u-8800-a001.prt-matsts_ss_316rho-8P1	7000002	1.86E-06	0.0249	2.177E-01	5.33E-04
s03050136-m8u-8800-a001-matsts_ss_316lrho-8P1	7000003	8.17E-06	0.0058	6.421E+00	2.35E-03
s03050136-m8u-8800-a001-matsts_ss_316lrho-82P1	7000004	4.35E-07	0.0169	3.508E-01	1.25E-04
pbw-proposal-1121.prt_pbw-proposal-1120-1-matsts_alu_6061-t6rho-2.7P1	7000005	1.15E-02	0.0009	8.911E+01	1.11E+00
s03050100-m8u-8800-a514-01.prt-matsts_alu_6061rho-2.7P1	7000006	7.63E-07	0.0829	3.866E-03	7.39E-05
s03050100-m8u-8800-a514-02.prt-matsts_ss_316rho-8P1	7000007	7.17E-07	0.0843	1.075E-02	2.04E-04
s03050142-m8u-8800-a001.prt--matsts_ss_316lrho-8P1	7000008	1.11E-05	0.0049	8.583E+00	3.18E-03
s03050141-m8u-8800-a001.prt-matsts_ss_316lrho-8P1	7000009	1.73E-05	0.0061	5.489E+00	4.95E-03
pbw-water-matsts_waterrho-0.997P1	7000010	2.74E-04	0.0012	1.248E+01	9.81E-03
pbw-proposal_around-1121.prt_pbw-proposal-1120-1-matsts_alu_6061-t6rho-2.7P1	7000011	8.46E-06	0.0055	4.978E+00	8.20E-04
s03050181-m8u-8800-a001.prt-matsts_ss_316lrho-8P1	7000012	7.79E-06	0.0028	7.163E+01	2.24E-03
cooled_colimator-matsts_316l_ss_90_h2o_10rho-7.299823P1	7000013	1.94E-05	0.0031	6.878E+01	5.09E-03
s03050141-m8u-8800-a001.prt2-matsts_ss_316lrho-8P1	7000014	2.80E-07	0.0247	8.452E-02	8.04E-05
aic-pbw-02_08_21-10610-03.prt-matsts_ss_316lrho-8P1	7000015	2.17E-07	0.0068	1.995E+00	6.24E-05
aic-pbw-02_08_21-10530.prt_pbw-04-11-2022-292-matsts_ss_316lrho-8P1	7000016	6.36E-08	0.0106	2.353E-01	1.83E-05
aic-pbw-02_08_21-10510-01.prt_pbw-04-11-2022-294-matsts_ss_316lrho-8P1	7000017	3.57E-07	0.0077	1.806E+00	1.02E-04
aic-pbw-02_08_21-10520-01.prt_pbw-04-11-2022-296-matsts_ss_316lrho-8P1	7000018	3.53E-07	0.0076	1.791E+00	1.01E-04
aic-pbw-02_08_21-10610-06.prt_pbw-04-11-2022-303-matsts_ss_316lrho-8P1	7000019	2.59E-08	0.0192	4.440E-02	7.45E-06
s03054002-m8u-8800-a001-as_fts.prt-matsts_ss_316rho-8P1	7000020	1.24E-06	0.0236	7.034E-02	3.30E-04
s03054003-m8u-8800-a001-as_fts.prt-matsts_ss_316rho-8P1	7000021	1.50E-07	0.0154	3.335E-01	4.30E-05

s03054005-m8u-8800-a001-as_fts.prt-matsts_ss_316rho-8-matsts_ss_316rho-8P1	7000022	3.46E-07	0.0397	8.903E-02	9.94E-05
s03054004-m8u-8800-a002-as_fts.prt-matsts_ss_316rho-8P1	7000023	3.90E-07	0.0371	9.120E-02	1.12E-04
s03054004-m8u-8800-a004.prt-matsts_ss_316rho-8P1	7000024	8.33E-08	0.0434	7.049E-02	2.39E-05
aic-harp-tube-out-liner-matsts_ss_316rho-8P1	7000025	3.98E-08	0.0589	1.692E-02	1.14E-05
sts-harp-evac-ftng-a002-1-02.prt_pbw-04-11-2022-566-matsts_ss_316rho-8P1	7000026	6.86E-08	0.068	1.306E-02	1.97E-05
sts-harp-evac-ftng-a002-1-03.prt_pbw-04-11-2022-567-matsts_ss_316rho-8P1	7000027	3.43E-08	0.0673	5.815E-03	9.86E-06
sts-harp-evac-ftng-a002-1-03.prt_pbw-04-11-2022-568-matsts_ss_316rho-8P1	7000028	3.25E-08	0.0567	5.502E-03	9.33E-06
sts-harp-evac-ftng-a002-1-02.prt_pbw-04-11-2022-569-matsts_ss_316rho-8P1	7000029	7.40E-08	0.0735	1.411E-02	2.13E-05
sts-harp-evac-ftng-a002-7-01.prt-matsts_ss_316rho-8P1	7000030	1.09E-07	0.0254	0.102226837	4.1912E-05
sts-harp-evac-ftng-a002-11-01.prt-matsts_ss_316rho-8P1	7000031	1.26E-07	0.0544	4.157E-02	3.62E-05
sts-harp-evac-ftng-a002-11-02.prt-matsts_ss_316rho-8P1	7000032	2.66E-07	0.0558	4.873E-02	7.64E-05
sts-harp-evac-ftng-a002-11-07.prt-matsts_ss_316rho-8P1	7000033	1.53E-07	0.0751	1.824E-02	4.38E-05
aic-pbw-02_08_21-10610-18.prt-matsts_ss_316rho-8P1	7000034	2.91E-08	0.0442	8.379E-03	8.36E-06
s0306-cv-weldment-53.prt-matsts_ss_316lrho-8P1	7000035	3.92E-06	0.0038	3.394E+01	1.13E-03
cam-inner-bridge-support4.prt-matsts_steel_a36rho-7.8P1	7000036	2.16E-07	0.0194	1.987E-01	6.05E-05
cam-pbw-mount-plate.prt-matsts_steel_a36rho-7.8P1	7000037	8.12E-08	0.0096	4.654E-01	2.27E-05
cam-level2-inner-shield2.prt-matsts_steel_a36rho-7.8P1	7000038	1.88E-07	0.0417	2.959E-02	5.25E-05
solid1-matsts_steel_a36rho-7.8P1	7200001	4.40E-08	0.008	1.492E+00	1.58E-06
s03061211-m8u-8800-a002-as_fts.prt_pbw-04-11-2022-1110-matsts_steel_a36rho-7.8P1	7200002	3.68E-09	0.0148	6.725E-02	1.32E-07
s03061212-m8u-8800-a002-as_fts.prt_pbw-04-11-2022-1111-matsts_steel_a36rho-7.8P1	7200003	2.34E-08	0.0116	4.244E-01	8.40E-07
s03061213-m8u-8800-a002-as_fts.prt_pbw-04-11-2022-1112-matsts_steel_a36rho-7.8P1	7200004	1.23E-08	0.0125	3.812E-01	4.42E-07
s03061214-m8u-8800-a002-as_fts.prt_pbw-04-11-2022-1113-matsts_steel_a36rho-7.8P1	7200005	1.23E-08	0.0114	3.826E-01	4.43E-07
s03061215-m8u-8800-a002-as_fts.prt_pbw-04-11-2022-1114-matsts_steel_a36rho-7.8P1	7200006	6.73E-09	0.0115	1.233E-01	2.41E-07

s03060211-m8u-8800-a004-as_fts.prt-matsts_steel_a36rho-7.8P1	7200007	3.07E-09	0.01	2.951E-01	1.10E-07
s03050304-m8u-8800-a001-as_fts.prt-matsts_steel_a36rho-7.8P1	7200008	4.25E-09	0.0077	4.534E-01	1.53E-07
s03060241-m8u-8800-a004-as_fts.prt-matsts_steel_a36rho-7.8P1	7200009	1.52E-08	0.0096	2.959E-01	5.47E-07
s03060242-m8u-8800-a004-as_fts.prt-matsts_steel_a36rho-7.8P1	7200010	4.57E-08	0.0102	6.572E-01	1.64E-06

Table 4: Average DPA in each part. The parts marked in purple are in Al6061-T6. For all other parts, the flux to DPA conversion factors for SS316 have been used.

Part name in SpaceClaim	F4 tally for neutron DPA	Relative Error [-]	F4 tally for proton DPA	Relative Error [-]	Average DPA per pulse	Average DPA per year
solid-matsts_316l_ss_90_h2o_10rho-7.299823P1	1.03E-02	0.0042	7.11E-05	0.0209	2.32E-12	6.26E-04
s03050121-m8u-8800-a001.prt-matsts_ss_316rho-8P1	1.21E-02	0.0113	3.45E-04	0.077	2.79E-12	7.53E-04
s03050136-m8u-8800-a001-matsts_ss_316lrho-8P1	4.28E-02	0.0047	6.76E-04	0.0177	9.73E-12	2.63E-03
s03050136-m8u-8800-a001-matsts_ss_316lrho-82P1	5.16E-03	0.0082	7.43E-05	0.054	1.17E-12	3.16E-04
pbw-proposal-1121.prt_pbw-proposal-1120-1-matsts_alu_6061-t6rho-2.7P1	6.85E-01	0.0041	3.46E+00	0.0002	9.29E-10	2.51E-01
s03050100-m8u-8800-a514-01.prt-matsts_alu_6061rho-2.7P1	1.69E-02	0.016	1.89E-05	0.3544	3.79E-12	1.02E-03
s03050100-m8u-8800-a514-02.prt-matsts_ss_316rho-8P1	9.28E-03	0.0223	2.10E-05	0.475	2.08E-12	5.62E-04
s03050142-m8u-8800-a001.prt--matsts_ss_316lrho-8P1	3.85E-02	0.0044	1.88E-03	0.0107	9.05E-12	2.44E-03
s03050141-m8u-8800-a001.prt-matsts_ss_316lrho-8P1	5.72E-02	0.005	2.97E-03	0.0136	1.35E-11	3.64E-03
pbw-proposal_around-1121.prt_pbw-proposal-1120-1-matsts_alu_6061-t6rho-2.7P1	5.08E-02	0.0039	4.99E-04	0.0135	1.15E-11	3.10E-03
s03050181-m8u-8800-a001.prt-matsts_ss_316lrho-8P1	3.34E-02	0.0036	2.41E-03	0.0045	8.01E-12	2.16E-03
cooled_colimator-matsts_316l_ss_90_h2o_10rho-7.299823P1	7.59E-02	0.0038	6.53E-03	0.0057	1.85E-11	4.99E-03
s03050141-m8u-8800-a001.prt2-matsts_ss_316lrho-8P1	4.57E-03	0.0103	1.35E-05	0.176	1.03E-12	2.77E-04
aic-pbw-02_08_21-10610-03.prt-matsts_ss_316lrho-8P1	6.29E-03	0.0048	7.47E-06	0.0533	1.41E-12	3.81E-04
aic-pbw-02_08_21-10530.prt_pbw-04-11-2022-292-matsts_ss_316lrho-8P1	1.81E-03	0.0073	1.86E-06	0.1705	4.06E-13	1.10E-04

aic-pbw-02_08_21-10510-01.prt_pbw-04-11-2022-294-matsts_ss_316lrho-8P1	8.05E-03	0.0049	1.60E-05	0.0508	1.81E-12	4.88E-04
aic-pbw-02_08_21-10520-01.prt_pbw-04-11-2022-296-matsts_ss_316lrho-8P1	8.07E-03	0.0048	1.73E-05	0.0484	1.81E-12	4.89E-04
aic-pbw-02_08_21-10610-06.prt_pbw-04-11-2022-303-matsts_ss_316lrho-8P1	8.19E-04	0.0121	2.04E-07	0.4485	1.83E-13	4.95E-05
s03054002-m8u-8800-a001-as_fts.prt-matsts_ss_316rho-8P1	4.40E-03	0.0124	1.35E-04	0.1181	1.02E-12	2.74E-04
s03054003-m8u-8800-a001-as_fts.prt-matsts_ss_316rho-8P1	2.87E-03	0.0077	9.02E-06	0.1174	6.45E-13	1.74E-04
s03054005-m8u-8800-a001-as_fts.prt-matsts_ss_316rho-8-matsts_ss_316rho-8P1	3.13E-03	0.0159	3.29E-05	0.1686	7.08E-13	1.91E-04
s03054004-m8u-8800-a002-as_fts.prt-matsts_ss_316rho-8P1	3.06E-03	0.0168	5.62E-05	0.2179	6.99E-13	1.89E-04
s03054004-m8u-8800-a004.prt-matsts_ss_316rho-8P1	1.53E-03	0.0149	6.66E-06	0.3292	3.44E-13	9.28E-05
aic-harp-tube-out-liner-matsts_ss_316rho-8P1	9.24E-04	0.0173	1.76E-06	0.5887	2.07E-13	5.60E-05
sts-harp-evac-ftng-a002-1-02.prt_pbw-04-11-2022-566-matsts_ss_316rho-8P1	1.18E-03	0.0205	2.99E-06	0.4126	2.64E-13	7.13E-05
sts-harp-evac-ftng-a002-1-03.prt_pbw-04-11-2022-567-matsts_ss_316rho-8P1	9.59E-04	0.0214	8.62E-07	0.7572	2.15E-13	5.80E-05
sts-harp-evac-ftng-a002-1-03.prt_pbw-04-11-2022-568-matsts_ss_316rho-8P1	9.80E-04	0.0215	2.85E-07	0.7996	2.20E-13	5.93E-05
sts-harp-evac-ftng-a002-1-02.prt_pbw-04-11-2022-569-matsts_ss_316rho-8P1	1.17E-03	0.0197	2.29E-06	0.4927	2.63E-13	7.09E-05
sts-harp-evac-ftng-a002-7-01.prt-matsts_ss_316rho-8P1	1.34E-03	0.0087	7.75E-06	0.1159	3.03E-13	8.18E-05
sts-harp-evac-ftng-a002-11-01.prt-matsts_ss_316rho-8P1	1.69E-03	0.0178	7.22E-06	0.3154	3.80E-13	1.02E-04
sts-harp-evac-ftng-a002-11-02.prt-matsts_ss_316rho-8P1	2.62E-03	0.021	8.57E-06	0.2284	5.88E-13	1.59E-04
sts-harp-evac-ftng-a002-11-07.prt-matsts_ss_316rho-8P1	1.73E-03	0.0261	9.98E-06	0.2906	3.91E-13	1.06E-04
aic-pbw-02_08_21-10610-18.prt-matsts_ss_316rho-8P1	8.60E-04	0.0166	4.92E-08	0.9787	1.93E-13	5.20E-05
s0306-cv-weldment-53.prt-matsts_ss_316lrho-8P1	3.16E-02	0.0038	1.53E-03	0.0065	7.41E-12	2.00E-03
cam-inner-bridge-support4.prt-matsts_steel_a36rho-7.8P1	8.23E-03	0.0064	1.92E-05	0.1053	1.85E-12	4.99E-04
cam-pbw-mount-plate.prt-matsts_steel_a36rho-7.8P1	3.37E-03	0.0054	2.16E-06	0.0954	7.56E-13	2.04E-04
cam-level2-inner-shield2.prt-matsts_steel_a36rho-7.8P1	7.14E-03	0.0096	1.38E-05	0.2122	1.60E-12	4.32E-04
solid1-matsts_steel_a36rho-7.8P1	1.70E-03	0.006	8.12E-07	0.0737	3.81E-13	1.03E-04
s03061211-m8u-8800-a002-as_fts.prt_pbw-04-11-2022-1110-matsts_steel_a36rho-7.8P1	1.28E-04	0.0105	6.01E-09	0.6762	2.88E-14	7.77E-06

s03061212-m8u-8800-a002-as_fts.prt_pbw-04-11-2022-1111-matsts_steel_a36rho-7.8P1	1.03E-03	0.0063	1.00E-06	0.1102	2.30E-13	6.21E-05
s03061213-m8u-8800-a002-as_fts.prt_pbw-04-11-2022-1112-matsts_steel_a36rho-7.8P1	4.56E-04	0.0068	2.63E-07	0.1367	1.02E-13	2.76E-05
s03061214-m8u-8800-a002-as_fts.prt_pbw-04-11-2022-1113-matsts_steel_a36rho-7.8P1	4.63E-04	0.0067	2.77E-07	0.1341	1.04E-13	2.80E-05
s03061215-m8u-8800-a002-as_fts.prt_pbw-04-11-2022-1114-matsts_steel_a36rho-7.8P1	2.62E-04	0.0079	3.67E-08	0.619	5.88E-14	1.59E-05
s03060211-m8u-8800-a004-as_fts.prt-matsts_steel_a36rho-7.8P1	9.56E-05	0.0106	1.10E-08	0.3657	2.14E-14	5.78E-06
s03050304-m8u-8800-a001-as_fts.prt-matsts_steel_a36rho-7.8P1	1.55E-04	0.0078	1.89E-08	0.4039	3.48E-14	9.38E-06
s03060241-m8u-8800-a004-as_fts.prt-matsts_steel_a36rho-7.8P1	6.16E-04	0.0078	1.55E-07	0.4287	1.38E-13	3.73E-05
s03060242-m8u-8800-a004-as_fts.prt-matsts_steel_a36rho-7.8P1	2.05E-03	0.0067	1.44E-06	0.0894	4.60E-13	1.24E-04

Table 5: He-production in all aluminum parts.

Part name in SpaceClaim	F4 tally for neutrons	Relative Error [-]	F4 tally for protons	Relative Error [-]	Average He-production per year [appm]
pbw-proposal-1121.prt_pbw-proposal-1120-1-matsts_alu_6061-t6rho-2.7P1	2.95E-05	0.0046	2.28E-03	0.0001	1.39E+02
s03050100-m8u-8800-a514-01.prt-matsts_alu_6061rho-2.7P1	1.29E-07	0.0578	1.72E-09	0.3742	7.89E-03
pbw-proposal_around-1121.prt_pbw-proposal-1120-1-matsts_alu_6061-t6rho-2.7P1	6.22E-07	0.0069	5.11E-08	0.0149	4.07E-02

6. IMPACT OF BEAM PROFILE

This analysis was executed in response to revision 1 of Neutronics Task Order 37. Section 6.1 and 6.2 were performed in April 2023 and September 2023, respectively.

6.1 ENERGY DEPOSITION WITH A 60 CM² AND 30 CM² SUPERGAUSSIAN PROFILE

In this section, we evaluate the effect of two beam profiles with a smaller beam footprint with a super-Gaussian beam profile. The results are summarized in Table 6 and Figure 11, including a comparison with the results of the previous sections with an octupole profile with a beam footprint of 90 cm^2. With a smaller beam footprint, a higher maximal energy deposition is expected, as can be observed from comparing the results with the two super-Gaussian profiles. While the octupole beam profile has a footprint of 90 cm^2, its profile has peaks that reach a similar current density as the super-Gaussian profile with a 60 cm^2 footprint. The maximal energy deposition is, therefore, similar for these two profiles. Because the total power in the beam remains constant regardless of the profile, the total power in the PBW and in the water inside the PBW is the same for all beam profiles.

For all beam profiles, detailed data for the energy deposition in the PBW and the water inside the PBW has been made available for further engineering analysis.

Table 6: Impact of beam profile on maximal energy deposition in the PBW and the total power in the PBW and its cooling water

	Octupole 90 cm^2	Supergaussian 60 cm^2	Supergaussian 30cm^2
Max energy deposition in PBW	5.4 J/cc/pulse	5.2 J/cc/pulse	10.2 J/cc/pulse
Total power in PBW	1.41 kW	Same (within 1%)	Same (within 1%)
Total power in water	187 W	Same (within 1%)	Same (within 1%)

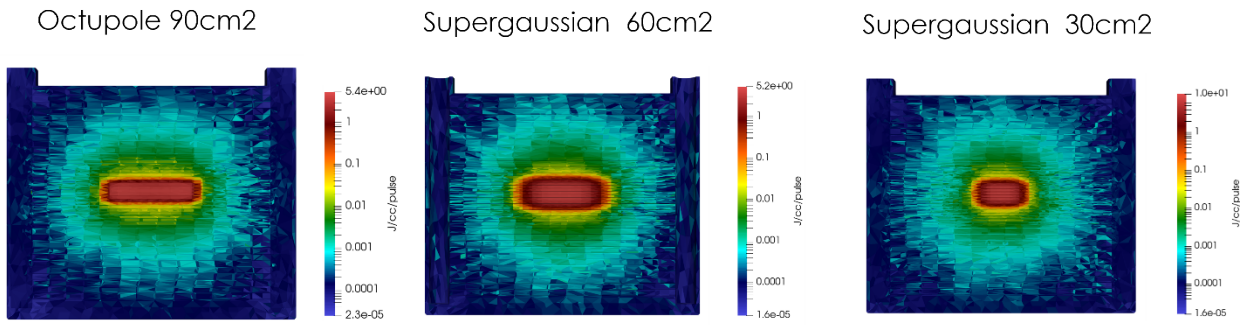

Figure 11: Energy deposition in a YZ plane through the middle of the PBW for different beam profiles.

6.2 PBW LIFETIME WITH A 60 CM² AND 30 CM² QUADRUPOLE PROFILE

With a more realistic quadrupole beam, the profile located at the PBW, which is ≈258 cm before the target face, can be very different from the profile at the target. To investigate the implications for the PBW lifetime, the helium production in the aluminum PBW is recalculated for two realistic beam profiles, with source terms derived from data received from the accelerator systems group. The first beam profile has a 90 cm^2 beam footprint on the target with a peak current density of ≈0.08 A/m^2 but reaches ≈0.137 A/m^2 at the location of the PBW. A second beam profile has a 60 cm^2 beam footprint on the target with a peak current density of ≈0.11 A/m^2, while the PBW sees a peak current density of ≈0.124 A/m^2. The results are summarized in Table 7 and visualized in Figure 12. The helium production rate is with 720 appm/year the highest for the 90 cm^2 quadrupole profile, which limits the PBW lifetime to 2.78 years. This is only slightly more limiting than the estimate with the 90 cm^2 octupole beam. It is noteworthy to point out that the maximal helium production rate is higher for the quadrupole beam profiles although their peak current densities are smaller than for the octupole beam profile. This is an effect of the different beam shape.

Table 7: Impact of beam profile on PBW lifetime

	Octupole 90 cm2 (2022)	Quadrupole 90 cm2 (2023)	Quadrupole 60 cm2 (2023)
Maximal heating	5.4 J/cc/pulse	6.0 J/cc/pulse	5.4 J/cc/pulse
Maximal helium production rate	660 appm/year	720 appm/year	680 appm/year
Lifetime based on helium production (max 2000 appm)	3.03 years	2.78 years	2.94 years
Peak current density at PBW	0.149 A/m^2	0.137 A/m^2	0.124 A/m^2

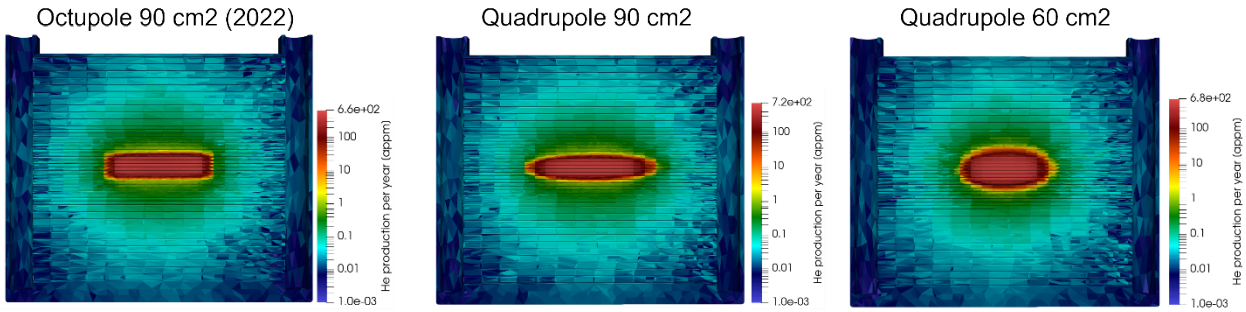

Figure 12: Helium production rates in a YZ plane through the middle of the PBW for different beam profiles.

7. CONCLUSIONS

We have analyzed the heating rates in the PBW assembly and the shielding above. Detailed data from unstructured mesh models have been made available for further analysis. Additionally, average heating rates per component have been calculated. Most of the analysis was performed for an octupole beam profile with a 90 cm^2 footprint. A few additional analyses have also been executed with different beam profiles.

We evaluated the dpa rates in all components of the PBW assembly, and the He-production rate in the aluminum components, such as the PBW. Detailed data from the unstructured mesh as well as averaged data for each component has been made available for further analysis.

An excellent agreement has been obtained comparing the maximum values of the heating rate, dpa, and He-production rates with previous results.

8. ACKNOWLEDGEMENTS

The author thanks Lukas Zavorka, Tucker McClanahan, Wouter de Wet and Igor Remec for their support.

9. REFERENCES

1. Personal communication with Igor Remec.

2. W. Lu, F.X. Gallmeier, P.J. Geoghegan, P.D. Ferguson and M.S. Wechsler, J. Nucl. Mater., 431 (2012) 33-38.

3. W. Lu, M. S. Wechsler, and Y. Dai, The NCSU Radiation Damage Database; Proton-Induced Damage Energy and Application to Radiation Damage at SINQ, J. Nucl. Mater., 356 (2006) 280-286.

4. W. Lu, M. S. Wechsler, P. D. Ferguson, and E. J. Pitcher, Spallation Radiation Damage Calculations and Database: Cross-Section Discrepancies between the Codes, J. ASTM Inter., Vol. 3, No. 7, 212-219, Paper ID JAI13467. Also available at http://www.astm.org/DIGITAL_LIBRARY/JOURNALS/JAI/PAGES/JAI13467.htm

5. W. Lu and M. S. Wechsler, The Radiation Damage Database: Section on Helium Cross Section, J. Nucl. Mater., 361 (2007) 282–288.

6. Joel A. Kulesza, Tucker C. McClanahan, "A Python Script to Convert MCNP Unstructured Mesh Elemental Edit Output Files to XML-based VTK Files ", LA-UR-19-20291 (2018).

APPENDIX A. COMPUTER HARDWARE AND SOFTWARE

APPENDIX A. COMPUTER HARDWARE AND SOFTWARE

Calculations have been run on Saturn with the following modules:

- Attila/10.1.2-dmp
- Mcnp/mcnp6.2mod_test

The octupole source starting 1060 cm upstream of the target has been used (octo_sampled_source_d_1060_cm_source_arrays.txt).

On Windows, ParaView 5.10.0-RC1 has been used for visualization.

APPENDIX B. LOCATION OF COMPUTATIONAL INPUT AND OUTPUT FILES

APPENDIX B. LOCATION OF COMPUTATIONAL INPUT AND OUTPUT FILES

All input and output files are archived in the sts-archive on Saturn: sts_archive/0-Task-Orders/TO-037_S.03.05_2022-04-05_PBW_HEATING/

APPENDIX C. FLUX TO DPA CONVERSION FACTORS

APPENDIX C. FLUX TO DPA CONVERSION FACTORS

In Figure 13, Figure 14, and Figure 15, the flux-to-dpa conversion factors are shown. Full details can be found in the MCNP input files.

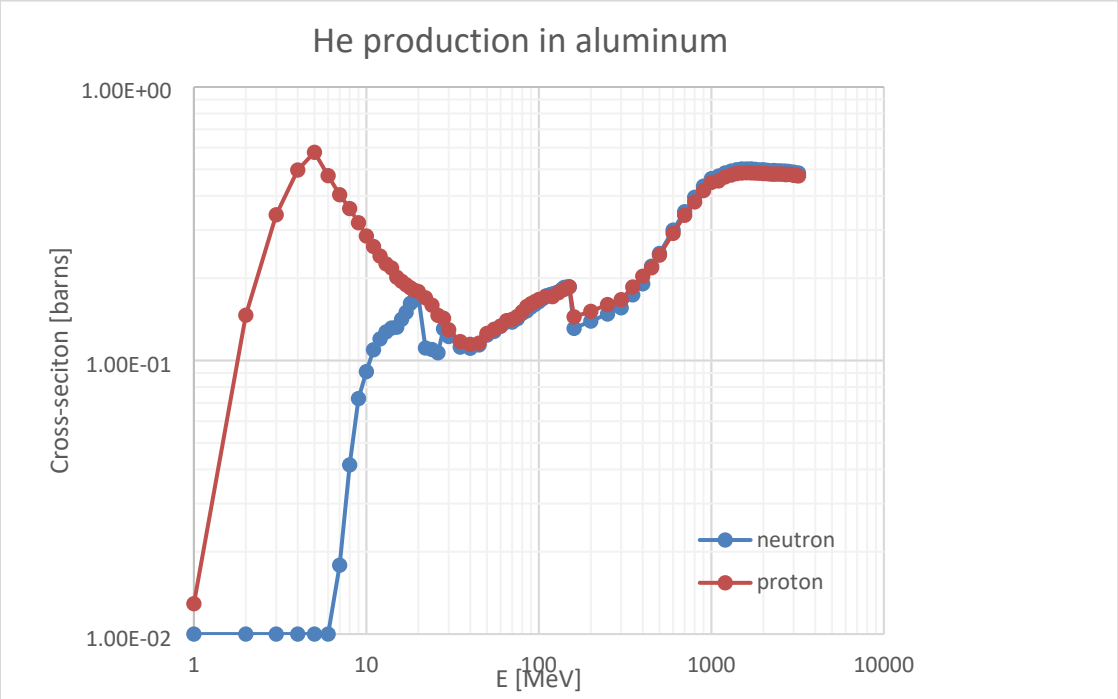

Figure 13: Flux-to-dpa conversion factors for He-production in aluminum. Values below 1e-2 barns are not shown.

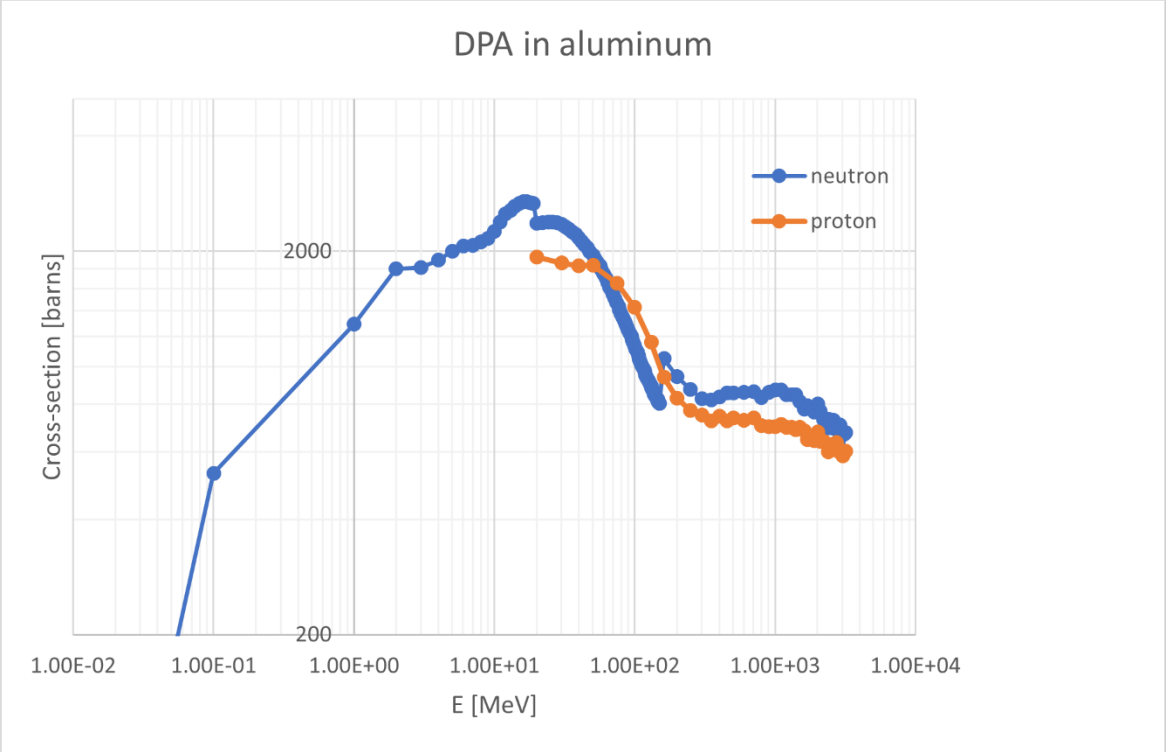

Figure 14: flux-to-dpa conversion factors for aluminum. Values smaller than 200 barns are not shown.

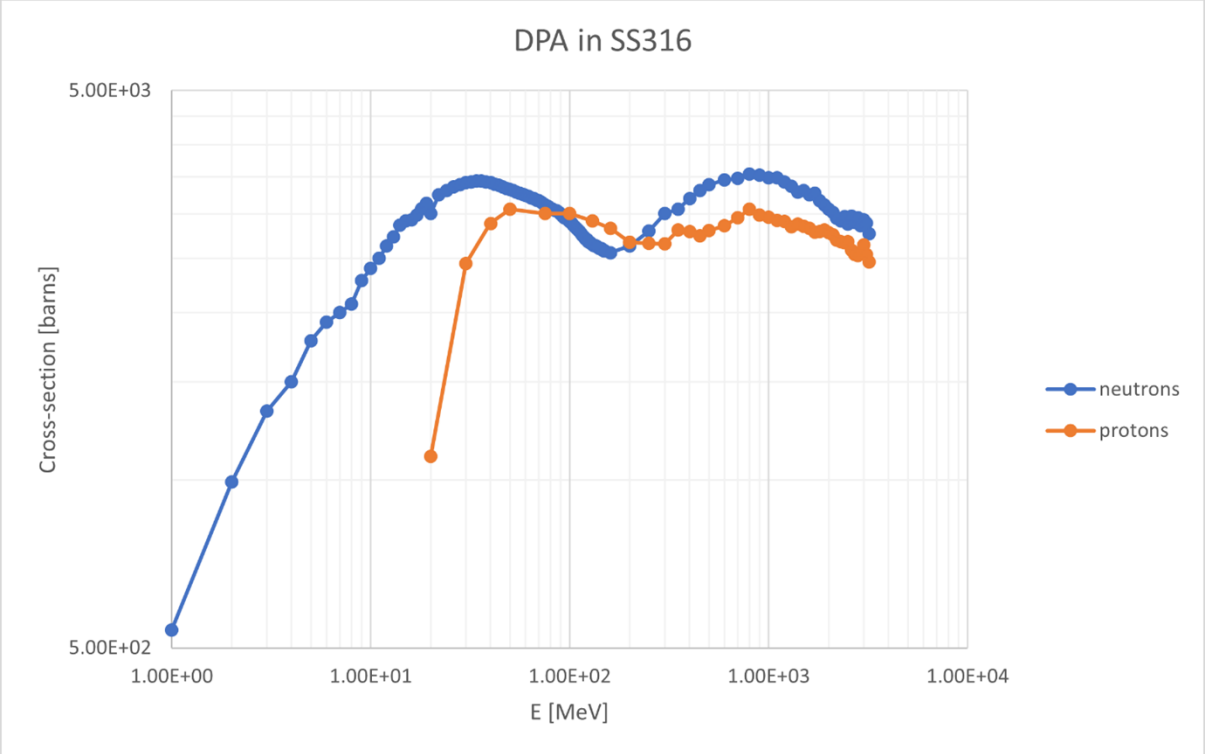

Figure 15: flux-to-dpa conversion factors for SS316. Values smaller than 500 barns are not shown.

APPENDIX D. VOLUME COMPARISONS

APPENDIX D. VOLUME COMPARISONS

In Table 8 and Table 9, we show volume comparisons between the parts in the original SpaceClaim file, the simplified SpaceClaim file, the unstructured mesh. Simplifications include reducing chamfers and filling small holes. To increase the resolution in the thin section of the PBW, this component has been separated from the thicker part of the PBW.

Table 8: Comparison of volumes of the parts in the simplified SpaceClaim and the original SpaceClaim

Part name in SpaceClaim	Volume in simplified SpaceClaim (cc)	Volume in original SpaceClaim (cc)	Percentage difference	Comment
Solid-mat:STS_316L_SS_90_H2O_10:rho-7.299823	6.50E-02	6.50E-02	-	
s03050121-m8u-8800-a001.prt-mat:STS_SS_316:rho-8	4.09E-04	3.80E-04	7.5	
s03050136-m8u-8800-a001-mat:STS_SS_316L:rho-8	2.74E-03	2.39E-03	14.69	roundings filled
s03050136-m8u-8800-a001-mat:STS_SS_316L:rho-8	2.81E-03	2.39E-03	17.7	roundings filled
pbw-proposal-1121.prt_pbw-proposal-1120-1-mat:STS_ALU_6061-T6:rho-2.7	8.02E-05			
Comment: Inside of the PBW is separated from outside to have different resolution in the parts (see underlined)				
s03050100-m8u-8800-a514-01.prt-mat:STS_ALU_6061:rho-2.7	2.61E-05	1.80E-05	45.4	roundings filled
s03050100-m8u-8800-a514-02.prt-mat:STS_SS_316:rho-8	2.61E-05	1.84E-05	42.07	roundings filled
Comment: 40% is a lot of difference and is better avoided. This component is a very small screw-like component on top of the PBW (left side). It is not important for the purpose of this analysis.				
s03050100-m8u-8800-a514-01.prt-mat:STS_ALU_6061:rho-2.7	2.61E-05	1.80E-05	45.4	roundings filled
s03050100-m8u-8800-a514-02.prt-mat:STS_SS_316:rho-8	2.61E-05	1.84E-05	42.07	roundings filled
Comment: 40% is a lot of difference and is better avoided. This component is a very small screw-like component on top of the PBW (right side). It is not important for the purpose of this analysis.				
s03050142-m8u-8800-a001.prt--mat:STS_SS_316L:rho-8	9.17E-04	8.70E-04	5.4	roundings filled
s03050141-m8u-8800-a001.prt-mat:STS_SS_316L:rho-8	1.11E-03	1.11E-03	-	
s03050142-m8u-8800-a001.prt--mat:STS_SS_316L:rho-8	9.17E-04	8.70E-04	5.4	roundings filled
PBW-water-mat:STS_WATER:rho-0.997	1.31E-03	1.31E-03	-0.23	
pbw-proposal_around-1121.prt_pbw-proposal-1120-1-mat:STS_ALU_6061-T6:rho-2.7	6.04E-03	6.05E-03	1.1	
s03050181-m8u-8800-a001.prt-mat:STS_SS_316L:rho-8	3.20E-02	3.16E-02	1.18	
Cooled Colimator-mat:STS_316L_SS_90_H2O_10:rho-7.299823	1.36E-02	1.36E-02	-	
s03050142-m8u-8800-a001.prt--mat:STS_SS_316L:rho-8	9.17E-04	8.70E-04	5.4	
s03050141-m8u-8800-a001.prt2-mat:STS_SS_316L:rho-8	1.06E-03	1.06E-03	-	

aic-pbw-02_08_21-10610-03.prt-mat:STS_SS_316L:rho-8	3.20E-02	3.08E-02	3.77	
aic-pbw-02_08_21-10530.prt_pbw-04-11-2022-292-mat:STS_SS_316L:rho-8	1.28E-02	1.28E-02	-	
aic-pbw-02_08_21-10510-01.prt_pbw-04-11-2022-294-mat:STS_SS_316L:rho-8	1.76E-02	1.69E-02	4.28	
aic-pbw-02_08_21-10520-01.prt_pbw-04-11-2022-296-mat:STS_SS_316L:rho-8	1.77E-02	1.70E-02	4.29	
aic-pbw-02_08_21-10610-06.prt_pbw-04-11-2022-303-mat:STS_SS_316L:rho-8	5.96E-03	5.70E-03	4.53	
s03054002-m8u-8800-a001-as_fts.prt-mat:STS_SS_316:rho-8	2.01E-04	2.97E-04	-32.42	Removed all curves
s03054003-m8u-8800-a001-as_fts.prt-mat:STS_SS_316:rho-8	7.79E-03	7.76E-03	0.29	
s03054005-m8u-8800-a001-as_fts.prt-mat:STS_SS_316:rho-8-mat:STS_SS_316:rho-8	4.51E-04	4.45E-04	1.44	
s03054004-m8u-8800-a002-as_fts.prt-mat:STS_SS_316:rho-8	7.88E-04	8.42E-04	-3.00	
s03054004-m8u-8800-a004.prt-mat:STS_SS_316:rho-8	2.96E-03	2.90E-03	1.94	
aic-harp-tube-out-liner-mat:STS_SS_316:rho-8	1.49E-03	1.49E-03	-	
sts-harp-evac-ftng-a002-1-02.prt_pbw-04-11-2022-566-mat:STS_SS_316:rho-8	6.64E-04	6.52E-04	1.82	
sts-harp-evac-ftng-a002-1-03.prt_pbw-04-11-2022-567-mat:STS_SS_316:rho-8	5.90E-04	5.79E-04	1.82	
sts-harp-evac-ftng-a002-1-03.prt_pbw-04-11-2022-568-mat:STS_SS_316:rho-8	5.90E-04	5.79E-04	1.82	
sts-harp-evac-ftng-a002-1-02.prt_pbw-04-11-2022-569-mat:STS_SS_316:rho-8	6.64E-04	6.52E-04	1.82	
sts-harp-evac-ftng-a002-7-01.prt-mat:STS_SS_316:rho-8	2.44E-03	2.44E-03	-	
sts-harp-evac-ftng-a002-11-01.prt-mat:STS_SS_316:rho-8	1.92E-04	1.91E-04	0.22	
sts-harp-evac-ftng-a002-11-02.prt-mat:STS_SS_316:rho-8	1.60E-04	1.58E-04	1.06	
sts-harp-evac-ftng-a002-11-01.prt-mat:STS_SS_316:rho-8	1.92E-04	1.91E-04	0.22	
sts-harp-evac-ftng-a002-11-01.prt-mat:STS_SS_316:rho-8	1.92E-04	1.91E-04	0.22	
sts-harp-evac-ftng-a002-11-02.prt-mat:STS_SS_316:rho-8	1.60E-04	1.58E-04	1.06	

sts-harp-evac-ftng-a002-11-07.prt-mat:STS_SS_316:rho-8	5.20E-05	5.02E-05	3.61	
sts-harp-evac-ftng-a002-11-07.prt-mat:STS_SS_316:rho-8	5.20E-05	5.02E-05	3.61	
sts-harp-evac-ftng-a002-11-07.prt-mat:STS_SS_316:rho-8	5.20E-05	5.02E-05	3.61	
sts-harp-evac-ftng-a002-11-07.prt-mat:STS_SS_316:rho-8	5.20E-05	5.02E-05	3.61	
sts-harp-evac-ftng-a002-11-01.prt-mat:STS_SS_316:rho-8	1.92E-04	1.91E-04	0.22	
sts-harp-evac-ftng-a002-11-02.prt-mat:STS_SS_316:rho-8	1.60E-04	1.58E-04	1.06	
sts-harp-evac-ftng-a002-11-01.prt-mat:STS_SS_316:rho-8	1.92E-04	1.91E-04	0.22	
sts-harp-evac-ftng-a002-11-01.prt-mat:STS_SS_316:rho-8	1.92E-04	1.91E-04	0.22	
sts-harp-evac-ftng-a002-11-02.prt-mat:STS_SS_316:rho-8	1.60E-04	1.58E-04	1.06	
sts-harp-evac-ftng-a002-11-07.prt-mat:STS_SS_316:rho-8	5.20E-05	5.02E-05	3.61	
sts-harp-evac-ftng-a002-11-07.prt-mat:STS_SS_316:rho-8	5.20E-05	5.02E-05	3.61	
sts-harp-evac-ftng-a002-11-07.prt-mat:STS_SS_316:rho-8	5.20E-05	5.02E-05	3.61	
sts-harp-evac-ftng-a002-11-07.prt-mat:STS_SS_316:rho-8	5.20E-05	5.02E-05	3.61	
aic-pbw-02_08_21-10610-18.prt-mat:STS_SS_316:rho-8	1.00E-03	9.81E-04	2.2	
s0306-cv-weldment-53.prt-mat:STS_SS_316L:rho-8	3.01E-02	3.01E-02	-0.04	
cam-pbw-mount-plate.prt-mat:STS_STEEL_A36:rho-7.8	2.05E-02	2.30E-02	-10.82	

Table 9: Comparison of volumes used in MCNP and the simplified SpaceClaim model

Part name in SpaceClaim	Volume in simplified SpaceClaim (cc)	Volume in MCNP (cc)	Percentage difference
solid-matsts_316l_ss_90_h2o_10rho-7.299823P1	6.50E+04	6.50E+04	-0.01%
s03050121-m8u-8800-a001.prt-matsts_ss_316rho-8P1	4.09E+02	4.09E+02	0.00%
s03050136-m8u-8800-a001-matsts_ss_316lrho-8P1	2.74E+03	2.74E+03	-0.11%
s03050136-m8u-8800-a001-matsts_ss_316lrho-82P1	2.81E+03	2.81E+03	-0.14%
pbw-proposal-1121.prt_pbw-proposal-1120-1-matsts_alu_6061-t6rho-2.7P1	8.02E+01	8.02E+01	0.00%
s03050100-m8u-8800-a514-01.prt-matsts_alu_6061rho-2.7P1	5.23E+01	5.23E+01	0.14%
s03050100-m8u-8800-a514-02.prt-matsts_ss_316rho-8P1	5.23E+01	5.27E+01	0.89%
s03050142-m8u-8800-a001.prt--matsts_ss_316lrho-8P1	2.75E+03	2.70E+03	-1.91%
s03050141-m8u-8800-a001.prt-matsts_ss_316lrho-8P1	1.11E+03	1.11E+03	-0.33%
pbw-water-matsts_waterrho-0.997P1	1.31E+03	1.27E+03	-2.78%
pbw-proposal_around-1121.prt_pbw-proposal-1120-1-matsts_alu_6061-t6rho-2.7P1	6.04E+03	6.07E+03	0.60%
s03050181-m8u-8800-a001.prt-matsts_ss_316lrho-8P1	3.20E+04	3.20E+04	0.21%
cooled_colimator-matsts_316l_ss_90_h2o_10rho-7.299823P1	1.36E+04	1.35E+04	-0.50%
s03050141-m8u-8800-a001.prt2-matsts_ss_316lrho-8P1	1.06E+03	1.05E+03	-0.44%
aic-pbw-02_08_21-10610-03.prt-matsts_ss_316lrho-8P1	3.20E+04	3.20E+04	0.00%
aic-pbw-02_08_21-10530.prt_pbw-04-11-2022-292-matsts_ss_316lrho-8P1	1.28E+04	1.29E+04	0.24%
aic-pbw-02_08_21-10510-01.prt_pbw-04-11-2022-294-matsts_ss_316lrho-8P1	1.76E+04	1.76E+04	0.01%
aic-pbw-02_08_21-10520-01.prt_pbw-04-11-2022-296-matsts_ss_316lrho-8P1	1.77E+04	1.77E+04	0.01%
aic-pbw-02_08_21-10610-06.prt_pbw-04-11-2022-303-matsts_ss_316lrho-8P1	5.96E+03	5.96E+03	0.00%
s03054002-m8u-8800-a001-as_fts.prt-matsts_ss_316rho-8P1	2.01E+02	2.13E+02	6.25%
s03054003-m8u-8800-a001-as_fts.prt-matsts_ss_316rho-8P1	7.79E+03	7.76E+03	-0.35%
s03054005-m8u-8800-a001-as_fts.prt-matsts_ss_316rho-8-matsts_ss_316rho-8P1	9.02E+02	8.96E+02	-0.70%
s03054004-m8u-8800-a002-as_fts.prt-matsts_ss_316rho-8P1	8.42E+02	8.12E+02	-3.58%
s03054004-m8u-8800-a004.prt-matsts_ss_316rho-8P1	2.96E+03	2.95E+03	-0.28%

aic-harp-tube-out-liner-matsts_ss_316rho-8P1	1.49E+03	1.48E+03	-0.53%
sts-harp-evac-ftng-a002-1-02.prt_pbw-04-11-2022-566-matsts_ss_316rho-8P1	6.64E+02	6.64E+02	0.00%
sts-harp-evac-ftng-a002-1-03.prt_pbw-04-11-2022-567-matsts_ss_316rho-8P1	5.90E+02	5.90E+02	0.00%
sts-harp-evac-ftng-a002-1-03.prt_pbw-04-11-2022-568-matsts_ss_316rho-8P1	5.90E+02	5.90E+02	0.00%
sts-harp-evac-ftng-a002-1-02.prt_pbw-04-11-2022-569-matsts_ss_316rho-8P1	6.64E+02	6.64E+02	0.00%
sts-harp-evac-ftng-a002-7-01.prt-matsts_ss_316rho-8P1	2435.7	2.44E+03	0.14%
sts-harp-evac-ftng-a002-11-01.prt-matsts_ss_316rho-8P1	1.15E+03	1.15E+03	-0.23%
sts-harp-evac-ftng-a002-11-02.prt-matsts_ss_316rho-8P1	6.40E+02	6.38E+02	-0.32%
sts-harp-evac-ftng-a002-11-07.prt-matsts_ss_316rho-8P1	4.16E+02	4.16E+02	0.05%
aic-pbw-02_08_21-10610-18.prt-matsts_ss_316rho-8P1	1.00E+03	1.00E+03	0.00%
s0306-cv-weldment-53.prt-matsts_ss_316lrho-8P1	3.01E+04	3.01E+04	0.00%
cam-inner-bridge-support4.prt-matsts_steel_a36rho-7.8P1	3.28E+03	3.28E+03	0.00%
cam-pbw-mount-plate.prt-matsts_steel_a36rho-7.8P1	2.05E+04	2.05E+04	0.00%
cam-level2-inner-shield2.prt-matsts_steel_a36rho-7.8P1	5.64E+02	5.64E+02	0.00%

APPENDIX E. STATISTICAL ERRORS

APPENDIX E. STATISTICAL ERRORS

In Figure 16, Figure 17, Figure 18, Figure 19, and Figure 20, the statistical errors are shown on the same data that has been plotted in the figures in the results section of this report.

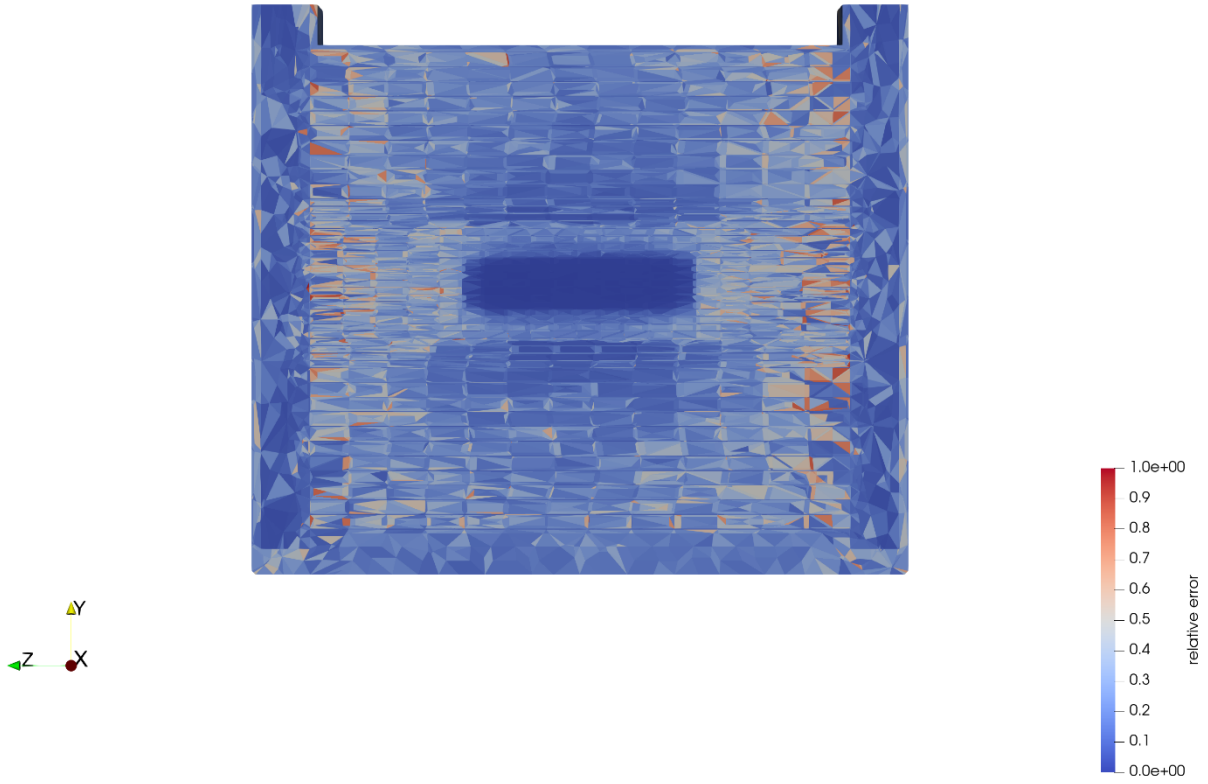

Figure 16: Statistical error on the energy deposition results in the PBW.

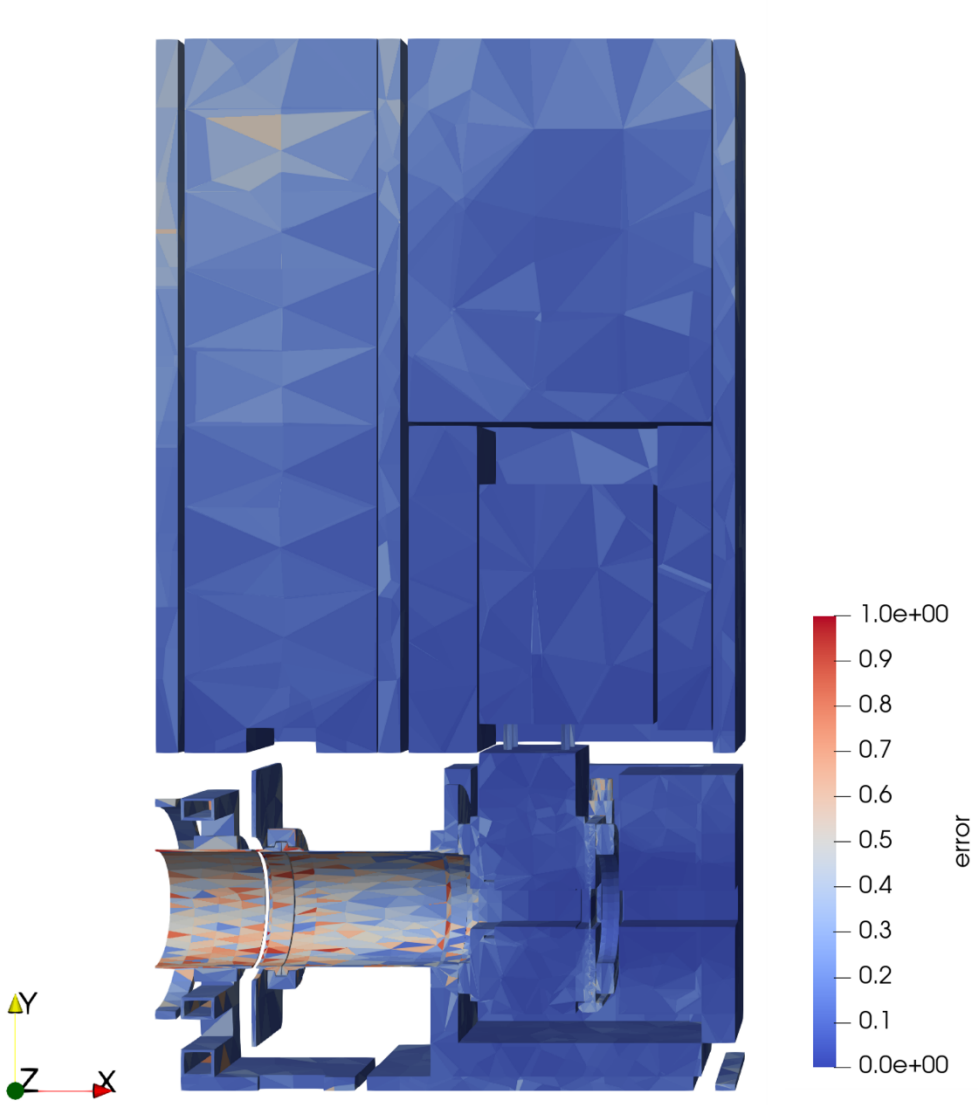

Figure 17: Statistical error on the energy deposition results.

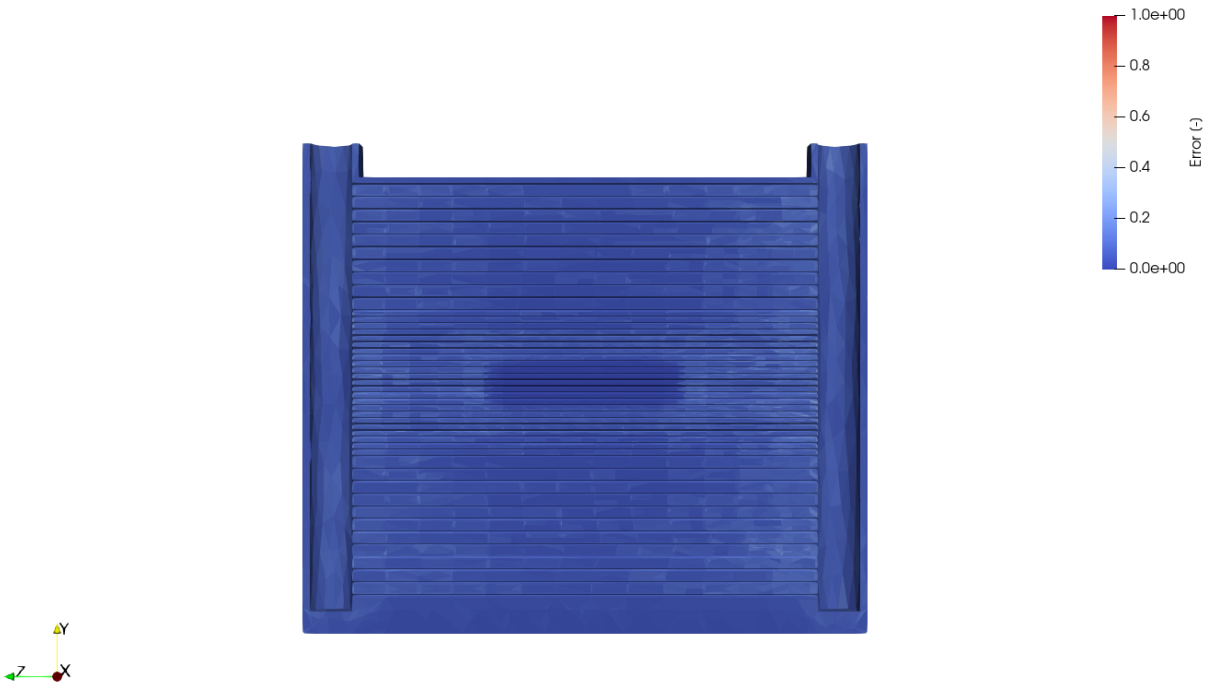

Figure 18: Statistical error for DPA in the PBW

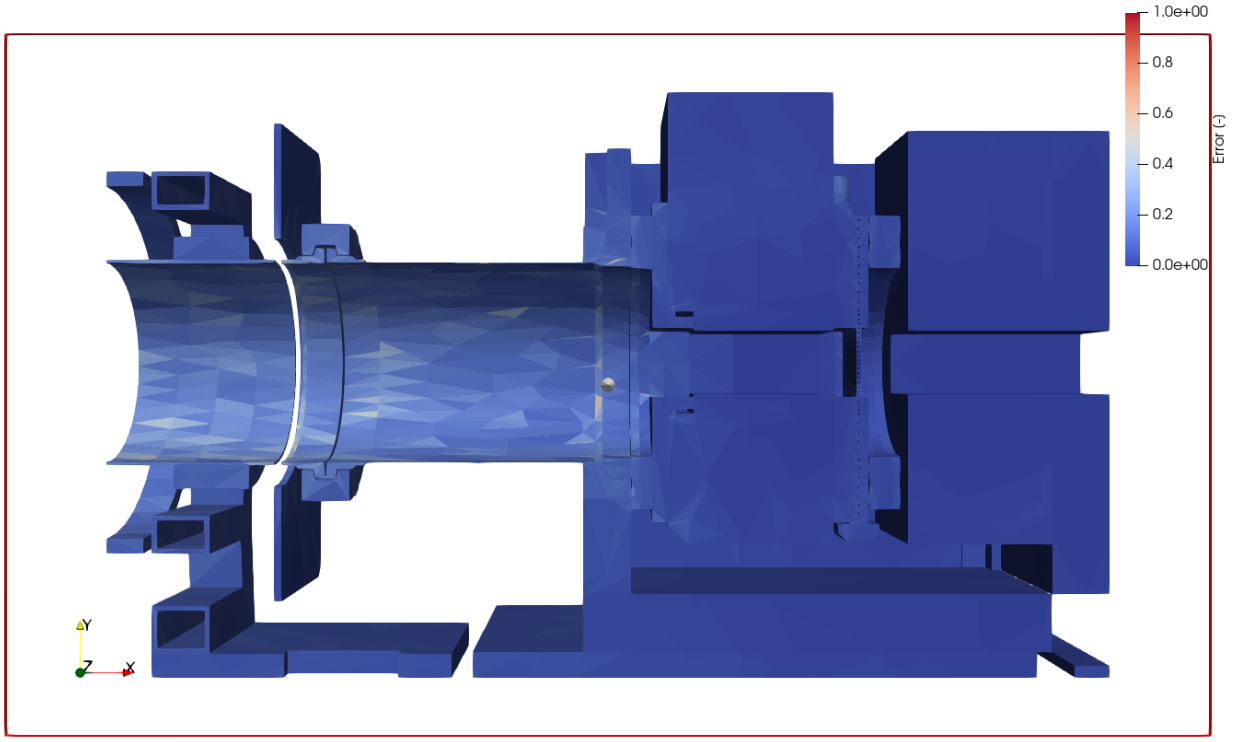

Figure 19: Statistical error for DPA in the PBW assembly

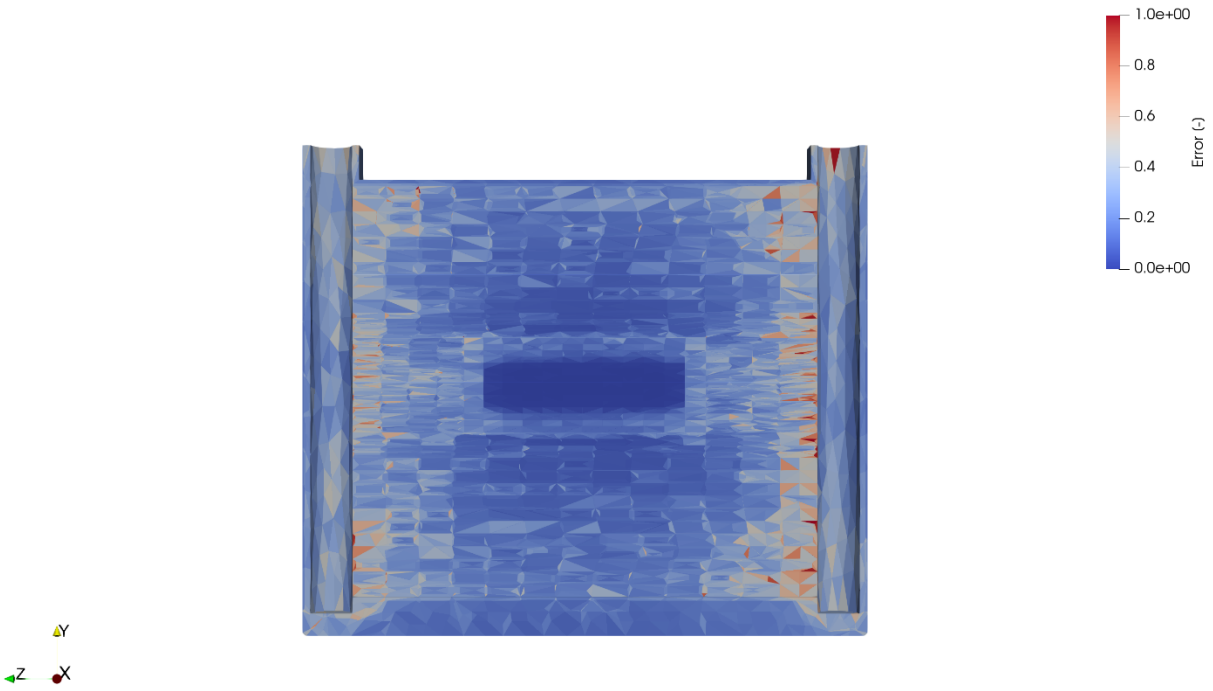

Figure 20: Statistical error for He-production in the PBW